

PLATOSpec's first results: Three new transiting warm Jupiters from the WINE survey TIC 147027702, TIC 245076932 and TIC 87422071

Pavol Gajdos^{1,2}, Rafael Brahm^{3,4}, Lorena Acuña-Aguirre⁵, Matías I. Jones⁶, Helem Salinas³, Jozef Lipták^{1,7}, Andrés Jordán^{3,4}, Thomas Henning⁵, Jiří Srba¹, Eva Žďárská¹, Zuzana Balkóová^{1,7}, Michaela Vítková^{1,8}, Jan Janík⁸, Petr Škoda¹, Jiří Žák¹, Djamel Mekarnia⁹, Olga Suarez⁹, Lyu Abe⁹, Matteo Beltrame^{10,11}, Amaury H.M.J. Triaud¹², Tristan Guillot⁹, Karen A. Collins¹³, Khalid Barkaoui^{14,15,16}, Gavin Boyle^{17,18}, Vincent Suc^{4,3,17}, Luca Antonucci^{19,20}, Marcelo Tala Pinto^{3,4}, Elizaveta Vostretcova²¹, Jan Eberhardt⁵, Néstor Espinoza²², Ismael Mireles²³, Pavel Pintr²⁴, Felipe I. Rojas²⁵, Veronika Schaffenroth²¹, Leo Vanzi^{19,20}, and Petr Kabáth¹

¹ Astronomical Institute, Czech Academy of Sciences, Fričova 298, 25165 Ondřejov, Czech Republic
e-mail: gajdos@asu.cas.cz

² Institute of Physics, Faculty of Science, Pavol Jozef Šafárik University, Park Angelinum 9, 04001 Košice, Slovakia e-mail: pavol.gajdos@upjs.sk

³ Facultad de Ingeniería y Ciencias, Universidad Adolfo Ibáñez, Av. Diagonal Las Torres 2640, Peñalolén, Santiago, Chile

⁴ Millennium Institute for Astrophysics, Av. Vicuña Mackenna 4860, 782-0436 Macul, Santiago, Chile

⁵ Max-Planck-Institut für Astronomie, Königstuhl 17, D-69117 Heidelberg, Germany

⁶ European Southern Observatory (ESO), Alonso de Córdova 3107, Vitacura, Casilla 19001, Santiago, Chile

⁷ Astronomical Institute of Charles University, V Holešovičkách 2, CZ-180 00 Prague, Czech Republic

⁸ Department of Theoretical Physics and Astrophysics, Faculty of Science, Masaryk University, Kotlářská 2, CZ-611 37 Brno, Czech Republic

⁹ Université Côte d'Azur, Observatoire de la Côte d'Azur, CNRS, Laboratoire Lagrange, CS 34229, F-06304 Nice Cedex 4, France

¹⁰ Istituto di Scienze Polari del CNR (ISP-CNR), Università Ca' Foscari, Via Torino n. 155, 30172 Venezia Mestre (VE), Italy

¹¹ Programma Nazionale di Ricerche in Antartide (PNRA), Institut polaire français Paul-Émile Victor (IPEV)

¹² School of Physics & Astronomy, University of Birmingham, Edgbaston, Birmingham B15 2TT, UK

¹³ Center for Astrophysics | Harvard & Smithsonian, 60 Garden Street, Cambridge, MA 02138, USA

¹⁴ Instituto de Astrofísica de Canarias (IAC), Calle Vía Láctea s/n, 38200, La Laguna, Tenerife, Spain

¹⁵ Astrobiology Research Unit, Université de Liège, 19C Allée du 6 Août, 4000 Liège, Belgium

¹⁶ Department of Earth, Atmospheric and Planetary Science, Massachusetts Institute of Technology, 77 Massachusetts Avenue, Cambridge, MA 02139, USA

¹⁷ El Sauce Observatory — Obstech, Coquimbo, Chile

¹⁸ Cavendish Laboratory, J. J. Thomson Avenue, Cambridge, CB3 0HE, UK

¹⁹ Center of Astro Engineering, Pontificia Universidad Católica de Chile, Av. Vicuña Mackenna 4860, 782-043 Santiago, Chile

²⁰ Department of Electrical Engineering, Pontificia Universidad Católica de Chile, Av. Vicuña Mackenna 4860, 782-043 Santiago, Chile

²¹ Thüringer Landessternwarte, D-07778 Tautenburg, Germany

²² Space Telescope Science Institute, 3700 San Martin Drive, Baltimore, MD 21218, USA

²³ Department of Physics and Astronomy, The University of New Mexico, Albuquerque, NM 87106, USA

²⁴ Institute of Plasma Physics of the Czech Academy of Sciences, Research Centre for Special Optics and Optoelectronic Systems TOPTEC, U Slovanky 2525/1a 182 00, Praha 8

²⁵ Instituto de Astrofísica, Pontificia Universidad Católica de Chile, Av. Vicuña Mackenna 4860, 7820436 Macul, Santiago, Chile

Received ; accepted

ABSTRACT

We report the discovery and characterisation of three transiting warm Jupiters: TIC 147027702b, TIC 245076932b and TIC 87422071b. These systems were initially identified as transiting candidates using light curves generated from the full-frame images of the TESS mission. We confirmed the planetary nature of these objects with ground-based spectroscopic follow-up observations using FEROS and the new PLATOSpec spectrograph attached to the ESO 1.52 m telescope at the La Silla Observatory, and with ground-based photometric observations of the Observatoire Moana, Las Cumbres Observatory Global Telescope and ASTEP. From a global fit to the photometry and radial velocities, we determine that the planet TIC 147027702b has a low-eccentric orbit ($e = 0.13 \pm 0.05$) with a period of 44.4 days and has a mass of $1.09^{+0.07}_{-0.13} M_J$ and a radius of $0.98 \pm 0.06 R_J$. TIC 245076932b has a moderately low mass of $0.51 \pm 0.05 M_J$, a radius of $0.97 \pm 0.05 R_J$, and an eccentric orbit ($e = 0.43 \pm 0.02$) with a period of 21.6 days. TIC 87422071b has a mass of $1.29 \pm 0.10 M_J$, a radius of $0.97 \pm 0.08 R_J$, and has a slightly eccentric orbit ($e = 0.12 \pm 0.07$) with a period of 11.3 days. These well-characterised warm Jupiters expand the currently limited sample of similar gas giants and provide valuable benchmarks for testing models of giant-planet formation, migration, and tidal evolution.

Key words. Techniques: photometric – Techniques: radial velocities – planetary systems – Planets and satellites: gaseous planets – Planets and satellites: detection

1. Introduction

The number of discovered exoplanets has increased over the years and currently exceeds 6,000. The majority of well-characterised giant planets are hot Jupiters - highly irradiated gas planets at extreme proximities from their host stars (e.g. Santerne et al. 2016). These planets are not expected to form at their current locations, given that the formation of planetary cores is highly inefficient inside the snowline (e.g. Rafikov 2005; Schlichting 2014). A possible mechanism to form the hot Jupiter population is migration from beyond the snowline, either by interactions with the gaseous disc when it is still present or through high eccentricity tidal migration mechanisms, generated by interactions with other objects in the system after the dispersal of the disc (e.g. Kley & Nelson 2012; Walsh et al. 2011).

Warm giant planets could be perceived as a transition state in the evolution of hot Jupiters. Warm Jupiters are generally defined as planets with masses greater than $0.3 M_J$ and orbital periods between 10 and 200 days (Dong et al. 2021). Their equilibrium temperatures are below ~ 1000 K. The observed properties, planetary atmospheres, and physical processes driving the structure of warm Jupiters are less affected by proximity to the host star, which makes them a unique opportunity to test planetary system formation and evolution theories. However, the number of discovered and well-characterised transiting warm giant planets is small – up to today, about 100^1 .

Here, we present the discovery, confirmation, and characterisation of three new transiting planets belonging to the class of warm Jupiters. They were identified as planetary candidates from the TESS light curves (Ricker et al. 2015) and confirmed by follow-up radial velocity measurement using the PLATOSpec spectrograph (Kab ath et al. 2026). In addition, we performed ground-based photometric observations to confirm the true source of the transit signal.

This paper is organised as follows. We describe the photometric and spectroscopic observations used in Sect. 2. Sec. 3 presents the stellar parameters of the parent star. In Sect. 4, we provide the parameters of the planetary system obtained by our analysis. Finally, we discuss our results and draw conclusions in Sect. 5.

2. Observations

2.1. TESS photometry

TIC 147027702b was identified as a transiting planetary candidate from the full-frame image (FFI) light curves of the TESS mission using a transformer-based algorithm (Salinas et al. 2025) in the context of the Warm gIaNts with tEss collaboration (WINE; Brahm et al. 2019; Jord an et al. 2020; Schlecker et al. 2020; Trifonov et al. 2021; Hobson et al. 2023; Eberhardt et al. 2023; Jones et al. 2024; Tala Pinto et al. 2025). The candidate was marked as a single transiter based on the observation from Sector 9 (March 2019). A posterior analysis revealed three additional transits in Sectors 10 (April 2019), 63 (March 2023), and 90 (March 2025). This target was also observed by TESS in Sector 36 (March 2021), but no transit occurred during that period. For the first two sectors (S9 and S10), the FFIs were collected with a cadence of 30 min. In Sectors 63 and 90, the cadence was changed to 200 seconds. The time series of these sectors are shown in Fig. 2. From these four TESS light curves, it was possible to constrain the orbital period of the transiting candidate to

$P \approx 44.4$ d. The transit depth of $\delta \approx 2200$ ppm, and therefore, is consistent with a possible warm giant planet.

Using a similar approach, a new transiting candidate was identified on the star TIC 245076932. However, multiple transits were detected in the light curves of the TESS primary mission, and the orbital period of the planetary candidate was estimated to be 21.6 days by Salinas et al. (2025). TESS observed this target during four sectors: Sector 11 (May 2019), Sector 37 (April 2021), Sector 38 (May 2021), and Sector 64 (April 2023). The cadence of FFIs in Sector 11 was 30 min. It was changed to 10 min in Sectors 37 and 38 and to 200 s in Sector 64. From their time series (Fig. 3), we identified 5 full transits with a depth of $\delta \approx 5990$ ppm. An additional partial transit was observed in Sector 11, where only the end of the engres is captured.

TIC 87422071 was identified as a planetary candidate with an orbital period of 11.36 days from the TESS quick-look pipeline (QLP, Huang et al. 2020). Seven transits in three TESS sectors (Fig. 4) were identified with a depth of $\delta \approx 4470$ ppm. Sector 13 (July 2019) has an FFIs cadence of 30 min. An additional two sectors, Sector 66 (June 2023) and Sector 93 (June 2025), were taken with a 200-s cadence.

Some additional out-of-transit variability can be observed in the LCs for each target, which varies between individual sectors. It is mainly the result of systematic trends in TESS data. There are significant differences in the amount of detrending comparing the used data product (QLP or SPOC). The SPOC pipeline eliminates most of the additional trends. Stellar variability (e.g. pulsations or stellar spots) has probably less impact in our case.

We analyse the target-pixel files (TPFs) for possible contamination from other sources. We have used `tpfplotter` (Aller et al. 2020) for this purpose. Figure 1 shows the TPF for all three targets. There are no neighbouring stars inside the aperture mask of TIC 147027702. Only a few fainter stars (with a brightness difference of more than 2 mag) were identified in the background with an angular separation from the target of at least $1.5'$. Inside the aperture mask of TIC 245076932, multiple faint stars can be identified. However, the brightness difference is 3 to 5 mag. TIC 87422071 has a close bright neighbour. The star TIC 87422067 (Gaia DR3 6721152024675106816) is separated by only $12''$ with a V mag of 12.82 (compared to 11.98 of our target). Ground-based photometry was therefore necessary to prove the real source of the transiting signal. The additional three stars fainter than 15.5 mag are presented in its aperture mask.

2.2. Ground-based photometry

We acquired ground-based photometric observations to confirm the true source of the transit signal. For this purpose, we used multiple telescopes in various observatories.

Observatoire Moana (OM) is a global network of small-aperture robotic optical telescopes. The station installed at the EL Sauce observatory in Chile consists of a 0.6 m Dall-Kirkham robotic telescope coupled to an Andor iKon-L 936 deep depletion $2k \times 2k$ CCD with a scale of $0.67''$ per pixel.

ASTEP (Antarctica Search for Transiting ExoPlanets) is a 40 cm telescope installed at the Concordia station on the Antarctic plateau (Dransfield et al. 2022; M ekarnia et al. 2016; Schmider et al. 2022). The FLI ProLine PL16801 4096 \times 4096 CCD camera has a field of view of $1^\circ \times 1^\circ$ and a scale of $0.92''$ per px.

The Las Cumbres Observatory Global Telescope (LCOGT) (Brown et al. 2013) 1.0m network node at South Africa Astronomical Observatory near Sutherland (SAAO) is equipped with a 4096 \times 4096 SINISTRO camera having an image scale of $0.389''$ per pixel, resulting in a $26' \times 26'$ field of view.

¹ Data from NASA Exoplanet Archive

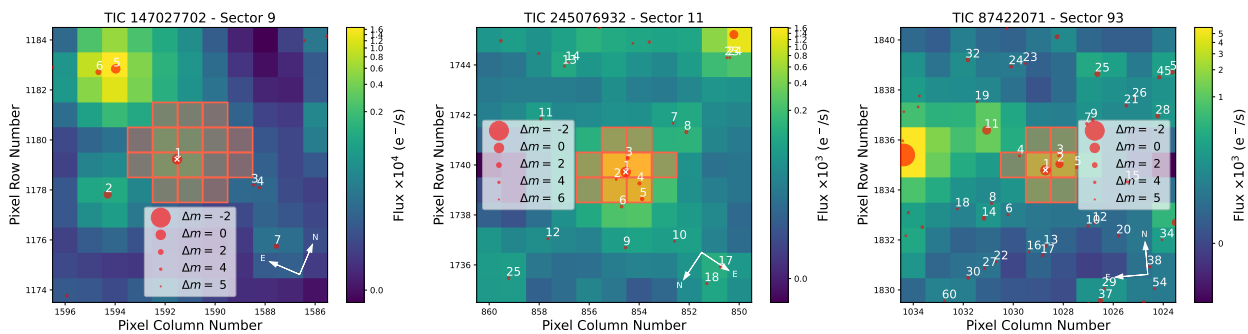


Fig. 1. TESS target pixel file (TPF) of TIC 147027702 (1st panel), TIC 245076932 (2nd panel) and TIC 87422071 (3rd panel).

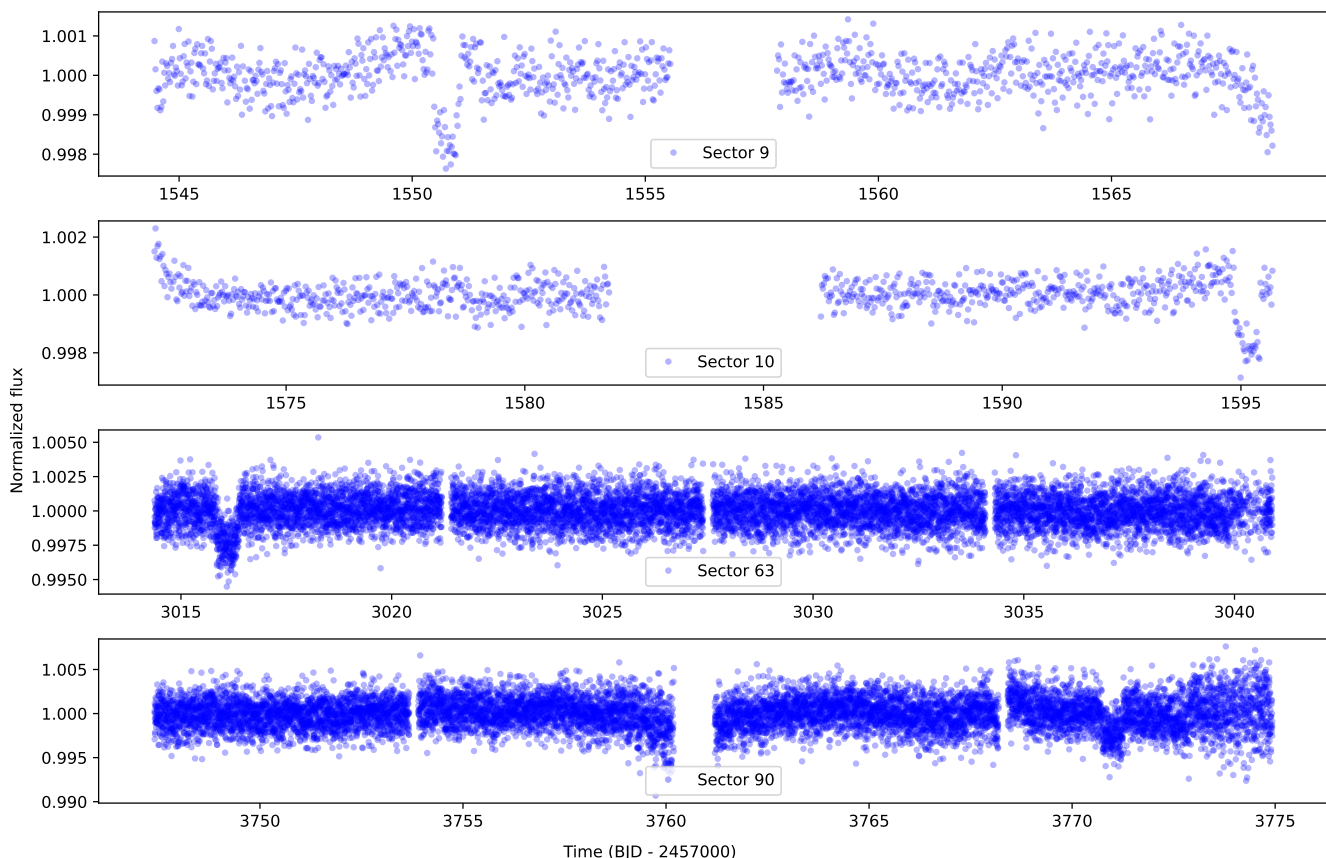


Fig. 2. TESS photometry of four sectors used in our analysis of TIC 147027702.

A transit of TIC 147027702 was observed with OMES during the night of 4/5 April 2025 using a Sloan r' filter and adopting exposure times of 16 s. The data were processed with an automated dedicated pipeline to deliver the relative photometric light curve of the event. This observation registered an ingress of the transit at the expected time. The light curve obtained, together with a theoretical one based on the model described in Sect. 4, is shown in Fig. 5.

A transit of TIC 245076932 was monitored with the ASTEP telescope during the night of 4/5 August 2025 using Johnson B and R filters. The adopted exposure time was 60 s in the B filter and 8 s in the R one. The complete transit was captured (see Fig. 5).

Two ground-based transits of TIC 87422071 were observed (see Fig. 6). We observed a full transit window on 27/28 May 2021 with the Sloan g' and Sloan i' bands from the LCOGT telescope. The images were calibrated using the standard LCOGT BANZAI pipeline (McCully et al. 2018) and differential photometric data were extracted using AstroImageJ (Collins et al. 2017). We used circular 5''8 photometric apertures that excluded flux from the nearest Gaia DR3 catalogue neighbour that is bright enough to possibly be the source of the TESS transit detection (Gaia DR3 6721152024675106816). We detected the transit in the target star photometric aperture in both bands, which confirms that the TESS-detected event is indeed occurring in TIC 87422071. Another partial transit was captured in

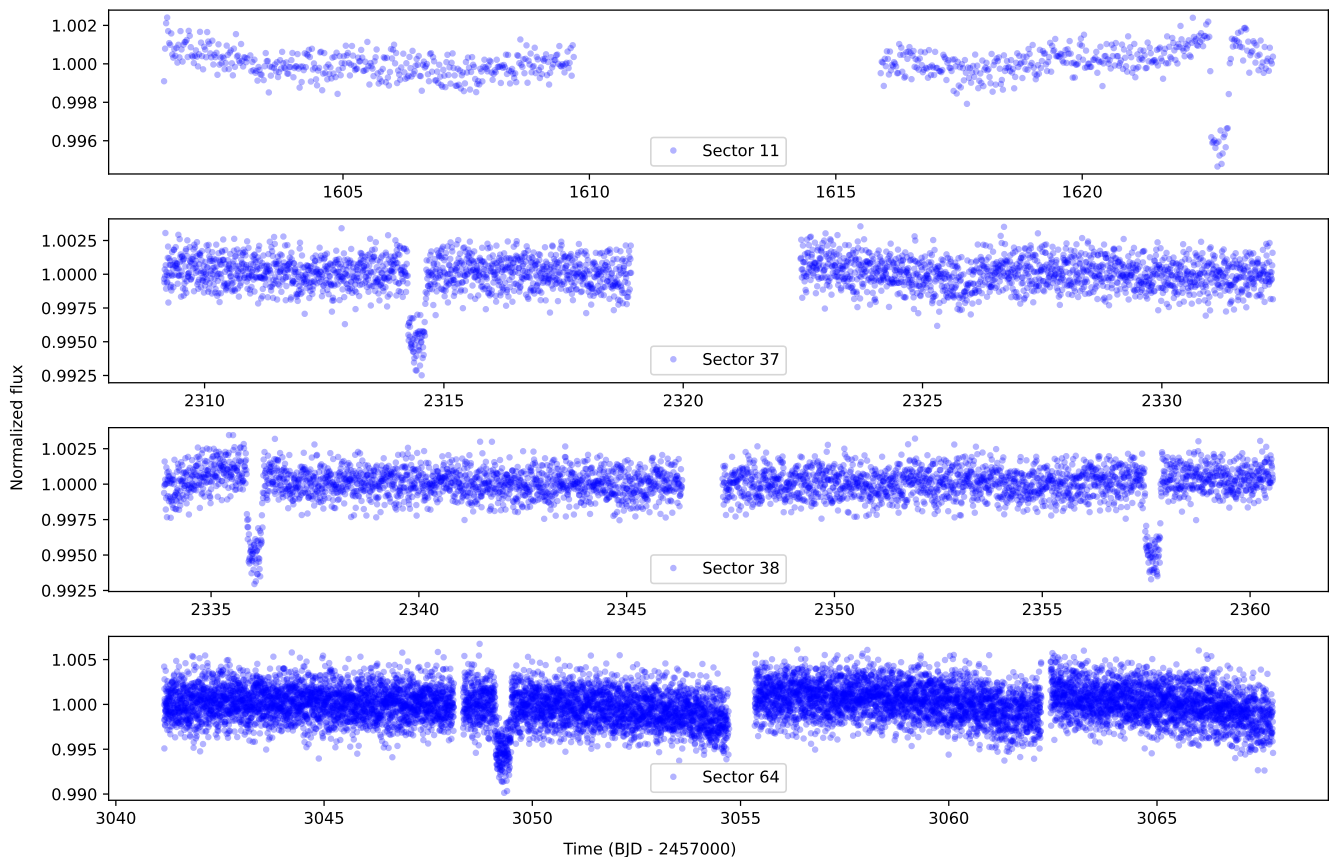


Fig. 3. TESS photometry of four sectors used in our analysis of TIC 245076932.

the Observatoire Moana during the night of 26/27 March 2024 using a Sloan r' filter and exposure times of 60 s. Photometric data were processed with the same pipeline as in the case of TIC 147027702.

In all three cases, we detected the transit exactly on the target studied. The shape and time of observed transit agree with the theoretical model as is clearly visible in Fig. 5 and 6.

2.3. Spectroscopy

We obtained follow-up radial velocities (RV) using the new PLATOSpec spectrograph (Kab ath et al. 2026). PLATOSpec is a white pupil echelle fibre-fed spectrograph with a spectral resolution power of $R = 70,000$ covering a wavelength range of 380 to 700 nm. PLATOSpec is attached to the ESO 1.52 m telescope at the La Silla Observatory, in Chile. Currently, the use of simultaneous calibrations using a Thorium-Argon (ThAr) lamp in a second fibre allows us to obtain RVs with a precision as good as 6 m/s for bright solar-type stars with slow projected rotational velocities. PLATOSpec data were processed with a modified version of the *ceres* pipeline (Brahm et al. 2017a), which performs all the reduction and processing steps required to obtain precision RVs starting from raw science and calibration images. RV measurements were calculated using cross-correlation with a G2-type star template. Besides precision RVs, the pipeline also delivers other outputs associated with the cross-correlation peak, like bisector span (BIS) and full-width at half maximum (FWHM) measurements.

We obtained 55 usable spectra of TIC 147027702 between January and July 2025 with a mean RV uncertainty of 26.6 m/s (listed in Tab. A.1), which was due to the moderate faintness and projected rotational velocity of the star. The observations were performed with exposure times of 20 and 30 minutes, depending on weather conditions. The average signal-to-noise ratio (SNR) per resolution element of these spectra was 42. A Generalized Lomb-Scargle (GLS) periodogram (Fig. 7) of the radial velocities shows a significant peak at ≈ 44.6 days, which is consistent with the orbital period of the candidate found from the TESS light curves. Additionally, we found no significant correlation between RVs and BIS (see Fig. B.1). RV measurements do not correlate with values of FWHM, CCF width or depth, or SNR (correlation coefficient less than 0.05).

We observed TIC 245076932 between February and August 2025 and collected 79 spectra suitable for the following analysis (listed in Tab. A.2). Observations performed with exposure times of 30 or 40 minutes resulted in a mean SNR of 34 and a mean RV uncertainty of 16.6 m/s. A significant peak at 21.4 days was detected in a GLS periodogram of RVs (Fig. 7), which is in good agreement with the orbital period detected by TESS photometry. An additional strong peak is visible at around 10.9 days, which is close to half of the main period. We found no significant correlation between RVs and BIS, FWHM, shape of CCF or SNR (correlation coefficient less than 0.1; see the relation for BIS in Fig. B.1).

For TIC 87422071, we obtained 43 spectra between May and August 2025 using PLATOSpec (listed in Tab. A.3). An expo-

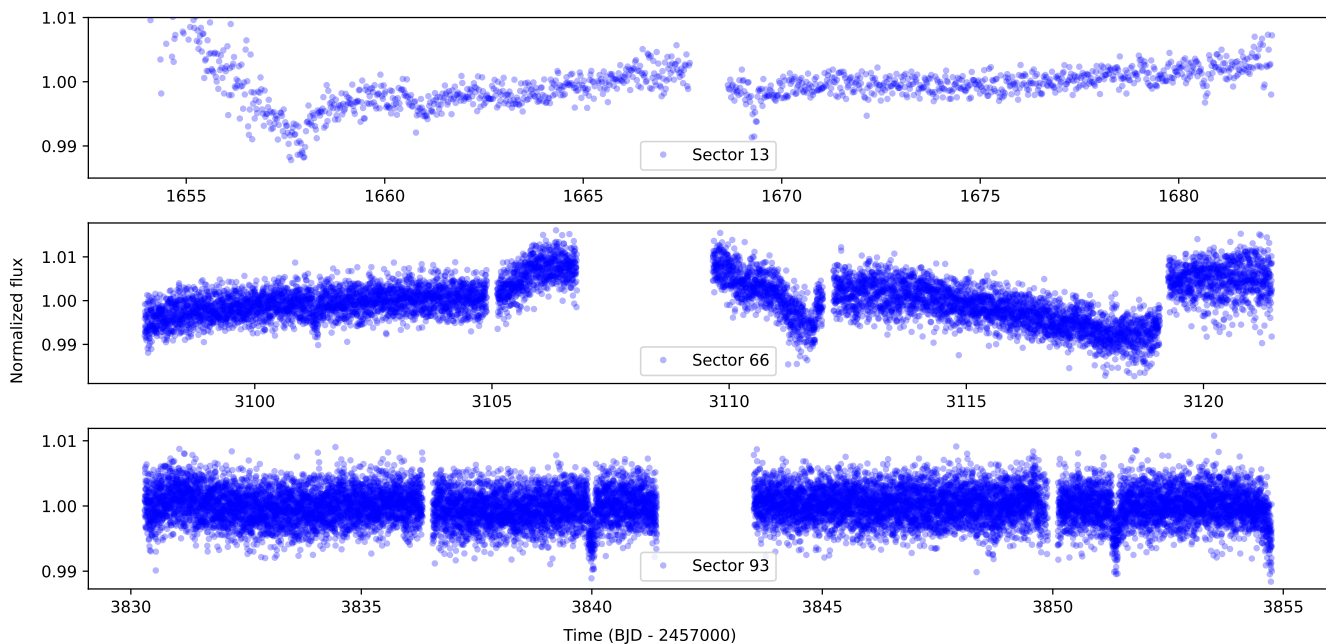


Fig. 4. TESS photometry of three sectors used in our analysis of TIC 87422071.

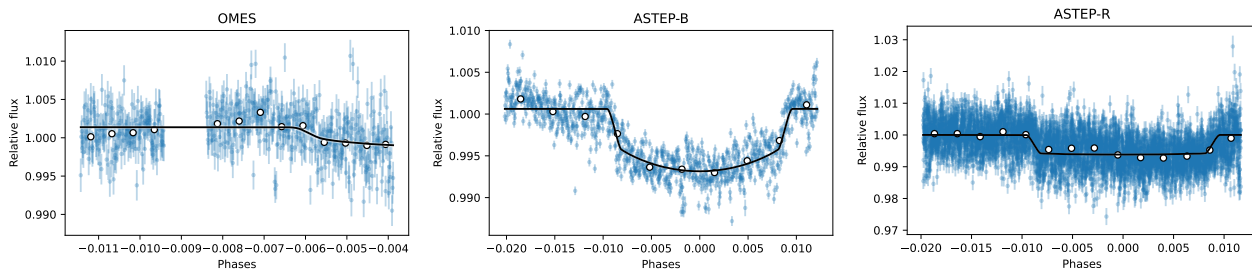


Fig. 5. Ground-based observation of transit of TIC 147027702 (*1st panel*) and TIC 245076932 in *B* filter (*2nd panel*) and *R* filter (*3rd panel*) with the best model (black). White points show the binned light curve.

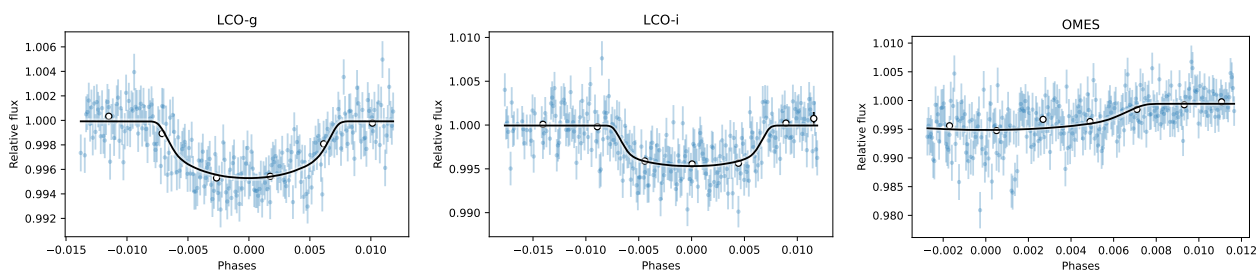


Fig. 6. Ground-based observations of transit of TIC 87422071 with the best model (black). White points show the binned light curve. *From left to right:* observation from LCO in *g'* filter and *i'* filter, observation from OMES in *r'* filter.

sure time of 40 minutes was used. The mean value of the RV uncertainty is 23.0 m/s, and the mean SNR is 33. Additionally, four spectra obtained by the FEROS spectrograph (Fiber-fed Extended Range Optical Spectrograph; Kaufer et al. 1999) in July 2024 and June 2025 with an exposure time of 20 minutes were used (see Tab. A.4). FEROS is a spectrograph that covers the range of 360 to 920 nm with a mean resolving power of $R = 48,000$ installed in the ESO-MPG 2.2 telescope at La Silla.

The mean SNR is 48 and the RV uncertainty is 17.2 m/s. Using the GLS periodogram of the RVs (Fig. 7), we detected a significant peak at 11.5 days very close to the photometric orbital period (11.36 days). A possible weak correlation between RVs and BIS could be observed (Fig. B.1; with a correlation coefficient of 0.4). This correlation is driven by two specific measurements obtained under poor observing conditions.

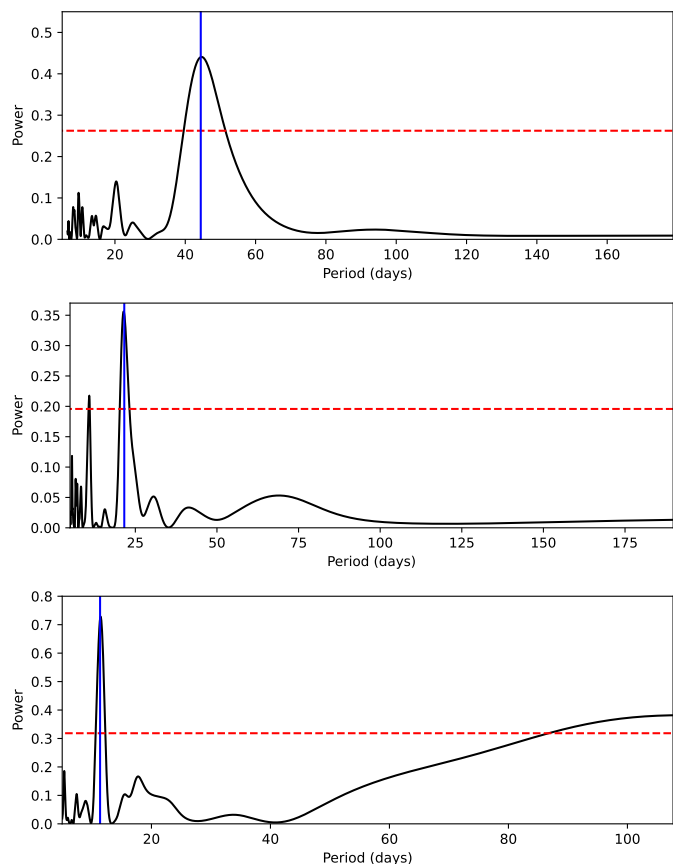


Fig. 7. Periodograms of RV data of TIC 147027702 (*top*), TIC 245076932 (*middle*) and TIC 87422071 (*bottom*). The horizontal red line corresponds to the 1% false alarm probability, and the blue line marks the orbital period determined from the photometric data.

3. Stellar parameters

We followed the same iterative procedure adopted in Brahm et al. (2023) to compute the atmospheric and physical parameters of the host star. We generated a co-added high SNR PLATOSpec spectrum of individual targets. We used the *zasp* code (Brahm et al. 2017b) to obtain a first estimation of the atmospheric parameters (T_{eff} , $\log g$, $[\text{Fe}/\text{H}]$, and $v \sin i$). Then we performed a spectral energy distribution (SED) fit to publicly available broadband photometry using the PARSEC stellar evolution models (Bressan et al. 2012) and the GAIA DR3 parallax (Gaia Collaboration 2023). In this step, we adopt the metallicity value found in our spectroscopic analysis. The SED fit delivers a more precise value for $\log g$, so we proceed with a new *zasp* run where $\log g$ is fixed to the value obtained with the SED fit. We keep iterating between these two procedures until we reach convergence in the derived atmospheric parameters of two contiguous *zasp* runs. To derive realistic uncertainties for the determined parameters, we adopted the procedure described in the paper of Tayar et al. (2022) and accordingly inflated the formal uncertainties obtained from our spectral modelling.

According to this modelling, TIC 147027702 is a slightly metal poor F-type dwarf star ($[\text{Fe}/\text{H}] = -0.08 \pm 0.05$ dex; $T_{\text{eff}} = 6410 \pm 183$ K) with a moderate projected rotational velocity of $v \sin i = 8.8 \pm 0.3$ km/s. TIC 245076932 is a late F-type dwarf star ($T_{\text{eff}} = 6130 \pm 178$ K) with a rotational velocity of $v \sin i = 4.2 \pm 0.3$ km/s close to the end of its life as a main-sequence star (age of about 4.5 Gyr). TIC 87422071 is a slightly

metal rich dwarf star of the F-type ($[\text{Fe}/\text{H}] = 0.16 \pm 0.05$ dex; $T_{\text{eff}} = 6150 \pm 178$ K), very similar to TIC 245076932 but 1 Gyr younger. Its rotational velocity is $v \sin i = 7.1 \pm 0.3$ km/s.

Table 1 shows the main stellar parameters of the targets and their identifiers in various catalogues. The sky coordinates (RA, Dec), the proper motion in both directions (μ_{α} , μ_{δ}) and the parallax π were obtained from Gaia DR3. All listed magnitudes (except for the *G* one) were collected from the TESS Input Catalog (TIC; Paegert et al. 2021).

4. Analysis and results

We performed a joint analysis of all photometric data (TESS and ground-based transits) and RV measurements using the *juliet* package (Espinoza et al. 2019) based on the packages *radvel* (RV modelling; Fulton et al. 2018) and *batman* (transit modelling; Kreidberg 2015).

The following set of planetary orbital parameters was used during the fitting routine as free ones: orbital period P , transit time t_0 , impact parameter $b \equiv a/R_{\star} \cos i$, radius ratio $p \equiv R_p/R_{\star}$, eccentricity e and argument of periastron ω (in forms $e \sin \omega$ and $e \cos \omega$), stellar density ρ_{\star} , and RV semi-amplitude K .

Each individual dataset is described by instrumental parameters. The relative flux offset μ and the jitter value σ were used in the case of photometric data. We also adopted a quadratic limb-darkening law with coefficients q_1 and q_2 . For RV measurements, we fitted instrumental systematic RV value μ and jitter σ .

Moreover, we utilised Gaussian processes (GP; Ambikasaran et al. 2015) to model stellar activity. We use this method only with TESS data. The GP are described by two parameters – amplitude σ_{GP} and time scale ρ_{GP} . We used a simple (approximate) Matern kernel implemented in the *celerite* package (Foreman-Mackey et al. 2017).

Tables 2, 3 and 4 list the priors of all fitted parameters for individual planetary candidates together with the median values of the posterior distributions. Uncertainties refer to the 1σ credibility interval.

The determined planetary parameters of all three systems are listed in Tab. 5. We derived additional parameters from the fitted ones. The derived parameters are orbital inclination i , semi-major axis a , planetary mass M_p and radius R_p , planet density ρ_p , surface gravity g_p , equilibrium temperature T_{eq} , transit depth δ and durations T_{14} and T_{23} . The equilibrium temperature was estimated under the assumption of zero albedo and perfect heat redistribution (Rodríguez Martínez et al. 2025). The best-fit model for the light curves of individual TESS sectors and phase-folded RV curves for individual systems are shown in Fig. 8, 9, and 10. Figures 5 and 6 show the model of the ground-based light curves.

According to our analysis, TIC 14027702b is a warm Jupiter with a mass of $1.09^{+0.07}_{-0.13} M_J$, a radius of $0.97 \pm 0.06 R_J$, and an orbital period of 44.4 days. The mean density of the planet is 1.44 g/cm^3 , and it has a low orbital eccentricity ($e = 0.127^{+0.055}_{-0.048}$). The equilibrium temperature is 863^{+26}_{-27} K.

TIC 245076932 is orbited by a warm Jupiter-type planet on a significantly eccentric orbit ($e = 0.428^{+0.022}_{-0.019}$) with a period of 21.6 days. The planet has a slightly lower density of $0.75 \pm 0.05 \text{ g/cm}^3$. Its radius is $0.97 \pm 0.05 R_J$ and has a mass of $0.51^{+0.04}_{-0.05} M_J$. The equilibrium temperature is similar to the previous one, 845 ± 25 K.

The third discovered warm Jupiter orbits star TIC 87422071 with an orbital period of 11.4 days on a low-eccentric ($e = 0.124^{+0.073}_{-0.060}$) orbit. The radius of the planet is $0.97 \pm 0.08 R_J$ and

Table 1. Stellar parameters and identifiers.

	TIC 147027702	TIC 245076932	TIC 87422071	Source
TIC ID	147027702	245076932	87422071	1
TOI	—	—	6752	1
TYC	7735-1496-1	8259-1806-1	7912-829-1	2
2MASS	J10470550-4355545	J13121527-5112519	J18120831-4414359	2
Gaia DR3	5390877409019489408	6080787214190400384	6721152093391972480	2
RA (J2000.0)	10h47m05.50s	13h12m15.28s	18h12m08.32s	3
Dec (J2000.0)	−43d55m54.58s	−51d12m51.99s	−44d14m35.95s	3
μ_α (mas/yr)	−11.805 ± 0.013	−24.412 ± 0.021	−9.263 ± 0.018	3
μ_δ (mas/yr)	7.228 ± 0.015	2.204 ± 0.017	−19.588 ± 0.014	3
π (mas)	2.1893 ± 0.0170	3.1788 ± 0.0226	2.5057 ± 0.0209	3
Distance (pc)	456.8 ± 3.5	314.7 ± 2.2	399.1 ± 3.3	5
T (mag)	10.630 ± 0.006	11.036 ± 0.006	11.194 ± 0.006	4
B (mag)	11.570 ± 0.122	12.203 ± 0.251	12.565 ± 0.322	4
V (mag)	11.286 ± 0.009	11.727 ± 0.017	11.982 ± 0.022	4
G (mag)	10.990 ± 0.003	11.463 ± 0.003	11.607 ± 0.003	3
J (mag)	10.110 ± 0.024	10.424 ± 0.024	10.588 ± 0.022	4
H (mag)	9.868 ± 0.026	10.155 ± 0.022	10.376 ± 0.023	4
K (mag)	9.801 ± 0.019	10.083 ± 0.019	10.223 ± 0.019	4
Luminosity (L_\odot)	6.80 ^{+0.52} _{−0.42}	2.11 ± 0.13	2.80 ^{+0.26} _{−0.21}	5
Mass (M_\odot)	1.406 ^{+0.074} _{−0.086}	1.117 ± 0.063	1.239 ^{+0.070} _{−0.080}	5
Radius (R_\odot)	2.136 ± 0.096	1.288 ± 0.058	1.489 ^{+0.072} _{−0.071}	5
ρ_\star (kg/m ³)	201.6 ^{+3.7} _{−2.2}	736.7 ^{+1.8} _{−1.3}	530.6 ^{+2.1} _{−1.8}	5
T_{eff} (K)	6410 ± 183	6130 ± 178	6150 ± 178	5
Age (Gyr)	2.7 ^{+0.7} _{−0.6}	4.5 ^{+1.3} _{−1.2}	3.5 ^{+1.3} _{−0.9}	5
log g (cm/s ²)	3.926 ± 0.020	4.267 ± 0.020	4.183 ^{+0.022} _{−0.023}	5
A_V (mag)	0.20 ^{+0.09} _{−0.08}	0.30 ^{+0.07} _{−0.08}	0.25 ± 0.11	5
[Fe/H] (dex)	−0.08 ± 0.05	0.02 ± 0.05	0.16 ± 0.05	5
$v \sin i$ (km/s)	8.8 ± 0.3	4.2 ± 0.3	7.1 ± 0.3	5
P_{rot} (upper limit) (days)	12.3 ± 0.6	15.5 ± 1.4	10.6 ± 0.7	5

References: (1) TESS (Ricker et al. 2015), (2) SIMBAD Database (Wenger et al. 2000), (3) Gaia DR3 (Gaia Collaboration 2023), (4) TIC v8.2 (Paegert et al. 2021), (5) this work.

has a mass of $1.29^{+0.10}_{-0.11} M_J$. The mean density is $1.88^{+0.33}_{-0.28} \text{ g/cm}^3$, and the equilibrium temperature is $1110 \pm 33 \text{ K}$.

4.1. Interior structure modelling

We perform an interior structure analysis for the three exoplanets. We use the GASTLI interior structure model (Acuña et al. 2021, 2025). GASTLI solves the one-dimensional equations of interior structure for exoplanets under the assumption that the interior is fully convective. The interior is divided into two layers: a heavy-element core composed of a 1:1 rock-water mixture and an envelope. The envelope consists of water (as a proxy for metals) and H/He at a cosmogonic mass ratio. For each of these materials – H/He, water, and rock – we employ up-to-date equations of state to calculate the density and entropy. Solving the equations of the interior structure of the planet requires defining the pressure and temperature in the outermost computational layer. To this end, we couple GASTLI to a grid of atmospheric models at a constant pressure of $P_{\text{surf}} = 1000 \text{ bar}$, which is high enough for atmospheric models (including the petitCODE grid we use) to solve for radiative transfer, as opacity tables range from low pressures (10^{-6} bar) to 1000 bar. This grid is the default GASTLI grid computed with the self-consistent 1D atmospheric model petitCODE (Mollière et al. 2015, 2017) for clear atmospheres in chemical equilibrium. petitCODE uses con-

vective adjustment to determine whether an atmospheric layer is convective or radiative, and calculates self-consistently the Bond albedo to estimate the energy balance at the top of the atmosphere. The GASTLI’s input parameters are the planetary mass, the core mass fraction (CMF), the atmospheric metallicity $\log(M/H)$ (expressed in solar units), the equilibrium temperature at the null Bond albedo $T_{\text{eq}}(A_B = 0)$, and the internal (or intrinsic) temperature T_{int} . The internal temperature is defined as the black-body temperature corresponding to the planet’s emission. As output, GASTLI computes the total planetary radius at the transit pressure in optical photometry (R_{planet} ; 20 mbar) and the age. The latter is calculated by solving the equation of thermal cooling for a luminosity $L = 4\pi R_{\text{planet}}^2 T_{\text{int}}^4$. In addition, the atmospheric metallicity $\log(M/H)$ is converted to envelope metal mass fraction Z_{env} by the atmospheric grid via chemical equilibrium. The total bulk metal mass fraction, Z_{planet} , is estimated to be $Z_{\text{planet}} = \text{CMF} + (1 - \text{CMF}) \times Z_{\text{env}}$. For more details on the GASTLI interior structure model, see Acuña et al. (2024).

We compute a grid for each of the three exoplanets at their respective equilibrium temperatures at the null Bond albedo. The grids span their $\pm 5\sigma$ mass interval with steps of $0.05 M_{\text{Jup}}$. The CMF ranges from 0 to 0.80 in steps of 0.10; $\log(M/H)$ ranges from -2 to 2 in steps of 1.0; and T_{int} ranges from 50 to 350 K in steps of 100 K. We linearly interpolate the grids to obtain the radius and the age for a set of input parameters, which to-

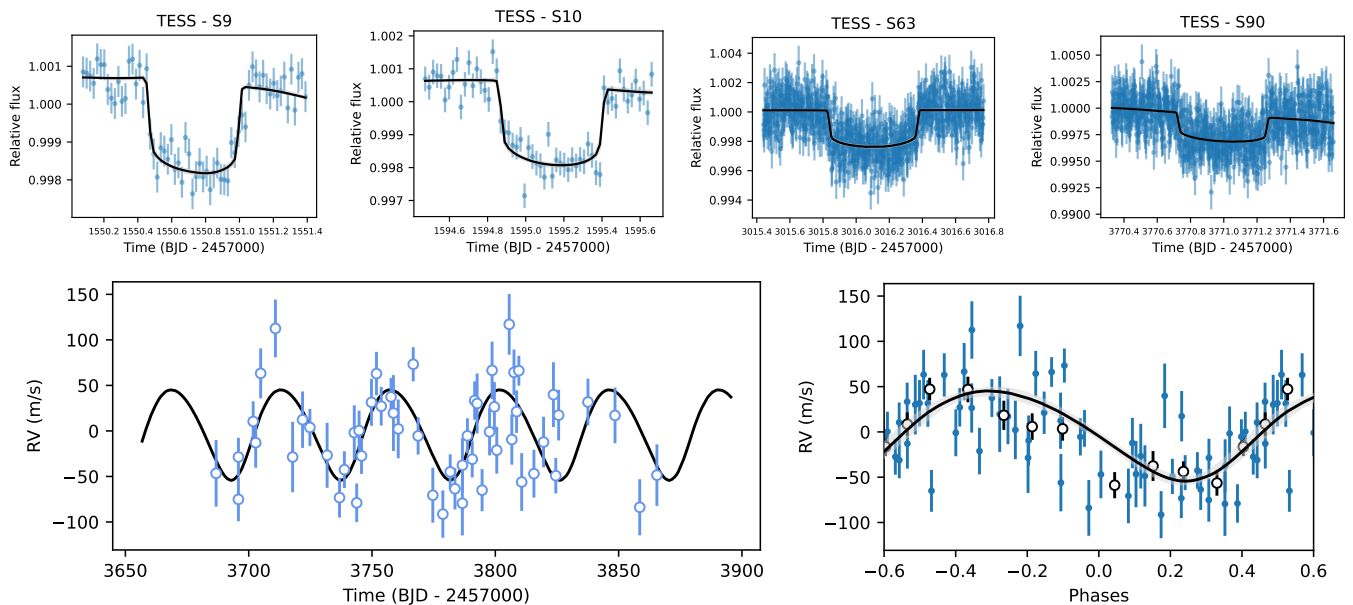


Fig. 8. *Top:* Light curves of TIC 147027702 for individual TESS sectors with the best model (black). *Bottom:* RV time series of TIC 147027702 and phase-folded RV curve with the best model (black). White points show the binned RV curve.

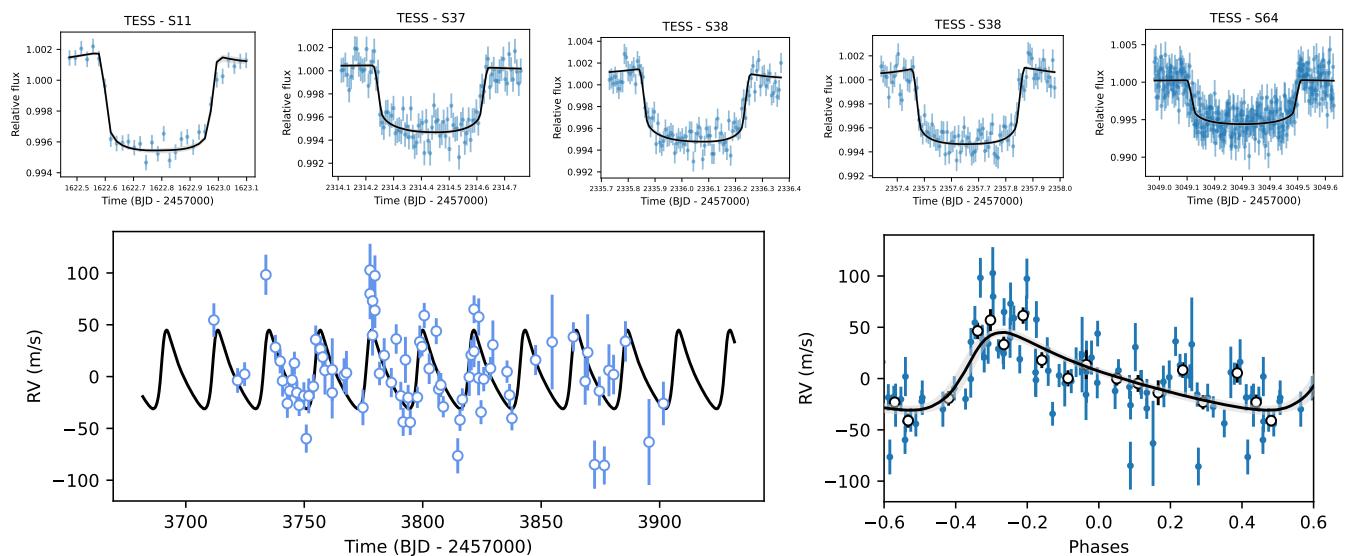


Fig. 9. Light curves and RV time series of TIC 245076932. For detail description see Fig. 8.

gether constitute the forward model in our retrievals. We use the Python package `emcee` (Foreman-Mackey et al. 2013) to sample the posterior distribution functions. In our retrievals, the mass, CMF, $\log(M/H)$, and T_{int} are free parameters. We adopt a Gaussian prior on the mass, with the mean and standard deviation set to the observed mean and the uncertainty values reported in Table 5. The parameters CMF, $\log(M/H)$, T_{int} have uniform priors: $\mathcal{U}(0, 0.8)$, $\mathcal{U}(-2, 2)$, $\mathcal{U}(50, 350)$, respectively. The likelihood function is evaluated from the squared residuals of the mass, radius, and age (Dorn et al. 2015; Acuña et al. 2021).

Table 6 shows the values retrieved from the compositional parameters for the three exoplanets. We estimate the planet-to-star bulk metal mass fraction ratio by dividing the retrieved Z_{planet} by the stellar metallicity, $Z_{\text{star}} = 0.0152 \cdot 10^{[\text{Fe}/\text{H}]_{\star}}$ (Tala Pinto et al. 2025). Fig. 11 shows the mass- $Z_{\text{planet}}/Z_{\text{star}}$ diagram

of the three exoplanets, including the two exoplanet population trends estimated by Thorngren et al. (2016) and Chachan et al. (2025). TIC 245076932 b and TIC 87422071 b are consistent with both trends in 1σ , while TIC 147027702 b is consistent with the fit of Chachan et al. (2025) in 2σ .

Additionally, TIC 245076932 b has a high eccentricity $e \sim 0.43$. The internal temperature of high-eccentricity exoplanets can be raised above the value predicted by secular cooling due to tidal heating (Leconte et al. 2010; Millholland et al. 2020). Radius inflation becomes significant at $T_{\text{eq}} > 1000$ K, well above the irradiation level of TIC 245076932 b. However, high internal temperatures ($T_{\text{int}} \sim 400$ K) have been observed in WASP-107 b and V1298 Tau b through disequilibrium chemistry and transmission spectroscopy (Sing et al. 2024; Welbanks et al. 2024; Barat et al. 2025). These two extrasolar gas giants have lower

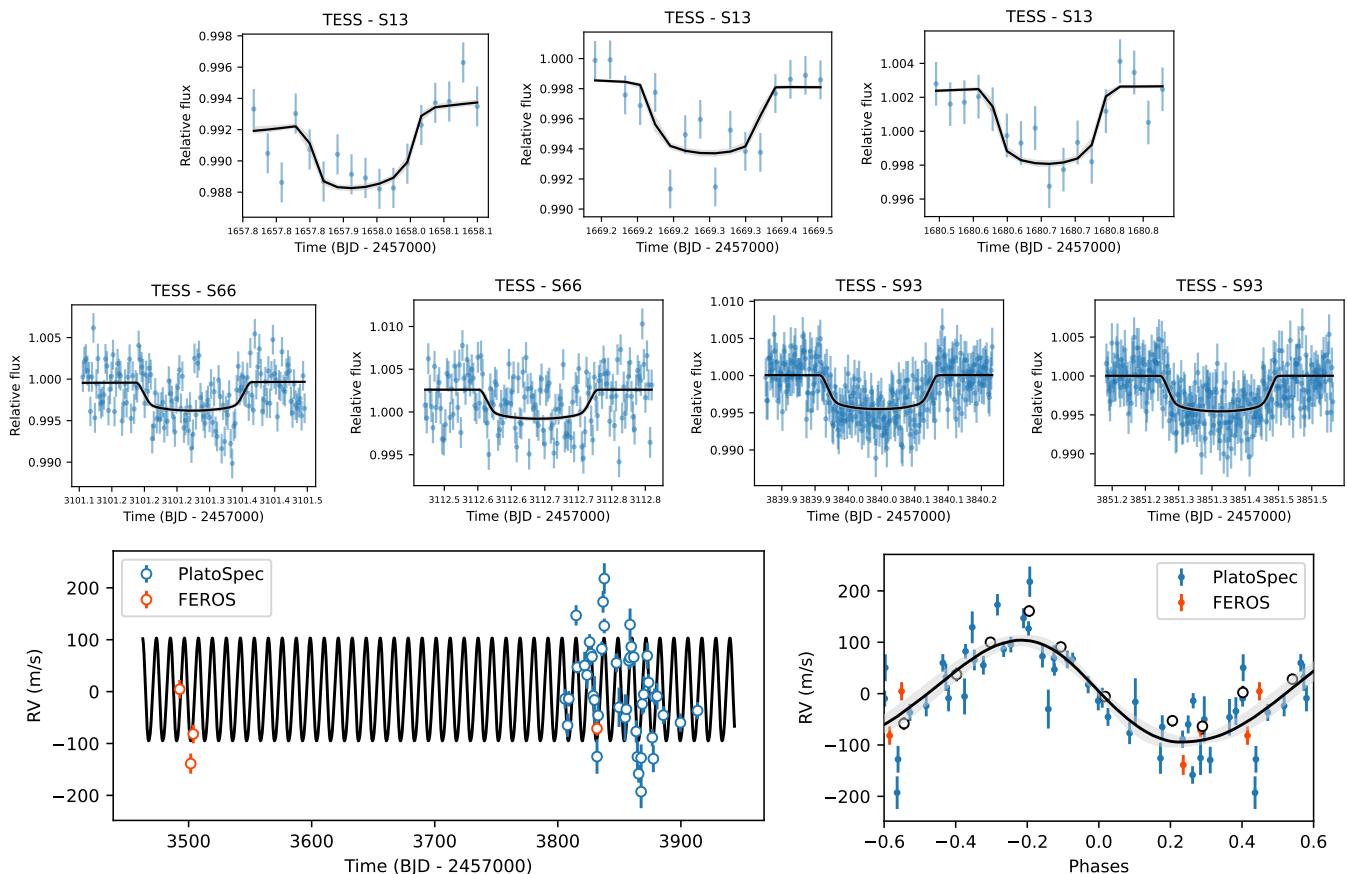


Fig. 10. Light curves and RV time series of TIC 87422071. For detail description see Fig. 8. Binned RV curve is calculated only using PLATOSpec data.

eccentricities than TIC 245076932 b, and it is currently debated whether their additional heating arises from Ohmic dissipation or from super-adiabatic regions induced by magnetic fields and compositional gradients, respectively (Barat et al. 2025; Batygin 2025). Thus, we consider an alternative scenario in which TIC 245076932 b has a high internal temperature $T_{\text{int}} = 350$ K. This scenario illustrates the effect of the heating mechanisms in inference of the compositional parameters. This scenario leads to a high core mass (M_{core}) and Z_{planet} , as the increase in T_{int} expands the radius of the planet, requiring a larger metal content to fit the observed mass and radius. In this case, we decouple T_{int} from the age by removing the age-squared residuals from the likelihood function in the retrieval.

Core accretion models predict core masses of at least $\sim 10 M_{\oplus}$ (Pollack et al. 1996). All three exoplanets have core masses above this threshold, consistent with an initial core formation stage followed by runaway gas accretion. However, TIC 245076932 b could have a core mass as low as $4 M_{\oplus}$ within 1σ . A refinement of the stellar age is required to rule out such a low core mass. If this were the case, TIC 245076932 b would not be consistent with the core accretion paradigm. Additionally, to determine whether these three exoplanets accreted solids during the runaway accretion phase, atmospheric characterisation would be required to estimate their atmospheric metallicities and carbon-to-oxygen ratios, which are valuable diagnostics of pebble and planetesimal accretion (Danti et al. 2023; Feinstein et al. 2025).

For comparison, we also computed the interior composition of the three planets using modules for experiments in astrophysics (MESA; Paxton et al. 2011, 2013). For this, we closely followed the implementation presented in Jones et al. (2024) and Tala Pinto et al. (2025), but with some minor modifications. In the case of TIC 147027702 b, we adopted the planetary envelope metallicity to be the same as that of the parent star, and we only varied the mass of the inert rocky core, whose density is estimated by assuming a 1:1 mixture of rock and ice (Hubbard & Marley 1989). On the other hand, for TIC 87422071 b, we increased the metallicity of the planet envelope to match its measured radius with our models, while the prescription to model the rocky core was identical to that for TIC 147027702 b. The results for these two planets are presented in Table 7. Finally, in the case of TIC 245076932 b, and given its small radius and high irradiation level, we could not find a satisfactory model that reproduces its observed properties.

5. Discussion and Conclusions

We report the discovery and characterisation of three warm Jupiter planets orbiting TIC 14027702, TIC 245076932 and TIC 87422071. These are the first exoplanets detected with the new temperature-stabilised spectrograph PLATOSpec (Kabáth et al. 2026). TIC 147027702b is a Jovian planet with a mass of $1.09 M_J$ and an orbital period of 45 days. With a time-averaged equilibrium temperature below 900 K, it fits the population of warm Jupiter planets. Planet TIC 245076932b has a significant

Table 2. Prior parameter distributions and median value of the posterior distributions of the fitted parameters of the joint transit and RV analysis of TIC 147027702.

Parameter	Distribution	Value
P (days)	$\mathcal{N}(44.405, 0.2)$	$44.405236^{+1.33e-4}_{-1.27e-4}$
$t_0 - 2457000$ (days)	$\mathcal{N}(1550.7, 0.2)$	$1550.73135^{+3.47e-3}_{-3.82e-3}$
$b \equiv a/R_\star \cos i$	$\mathcal{U}(0, 1)$	$0.230^{+0.145}_{-0.155}$
$p \equiv R_p/R_\star$	$\mathcal{U}(0.001, 0.1)$	$0.0469^{+0.0009}_{-0.0010}$
$e \sin \omega$	$\mathcal{U}(-0.8, 0.8)$	$-0.076^{+0.026}_{-0.048}$
$e \cos \omega$	$\mathcal{U}(-0.8, 0.8)$	$-0.087^{+0.050}_{-0.050}$
ρ_\star (kg/m ³)	$\mathcal{N}(200, 15)$	$201.55^{+3.67}_{-2.17}$
K (m/s)	$\mathcal{U}(0, 100)$	$50.43^{+1.36}_{-3.61}$
$\mu_{\text{PlatoSpec}}$ (m/s)	$\mathcal{U}(22500, 23000)$	$22753.56^{+5.72}_{-2.68}$
$\sigma_{\text{PlatoSpec}}$ (m/s)	$\mathcal{J}(0, 1000)$	$16.39^{+1.70}_{-1.70}$
$q_{1,\text{TESS}}$	$\mathcal{U}(0, 1)$	$0.14^{+0.18}_{-0.08}$
$q_{2,\text{TESS}}$	$\mathcal{U}(0, 1)$	$0.42^{+0.36}_{-0.20}$
$q_{1,\text{ground-r}}$	$\mathcal{U}(0, 1)$	$0.66^{+0.24}_{-0.39}$
$q_{2,\text{ground-r}}$	$\mathcal{U}(0, 1)$	$0.33^{+0.35}_{-0.24}$
$\mu_{\text{TESS-S9}}$	$\mathcal{N}(0, 0.1)$	$-1.04e-4^{+9.28e-4}_{-5.86e-4}$
$\mu_{\text{TESS-S10}}$	$\mathcal{N}(0, 0.1)$	$-2.83e-4^{+11.72e-4}_{-10.92e-4}$
$\mu_{\text{TESS-S63}}$	$\mathcal{N}(0, 0.1)$	$-1.08e-4^{+0.66e-4}_{-0.49e-4}$
$\mu_{\text{TESS-S90}}$	$\mathcal{N}(0, 0.1)$	$-2.00e-4^{+6.87e-4}_{-7.57e-4}$
$\mu_{\text{ground-r}}$	$\mathcal{N}(0, 0.1)$	$-13.75e-4^{+1.29e-4}_{-1.42e-4}$
$\sigma_{\text{TESS-S9}}$	$\mathcal{J}(0.1, 1000)$	$1.89^{+0.79}_{-1.58}$
$\sigma_{\text{TESS-S10}}$	$\mathcal{J}(0.1, 1000)$	$218.29^{+2.72}_{-2.25}$
$\sigma_{\text{TESS-S63}}$	$\mathcal{J}(0.1, 1000)$	$3.46^{+3.44}_{-2.04}$
$\sigma_{\text{TESS-S90}}$	$\mathcal{J}(0.1, 1000)$	$2.87^{+1.58}_{-2.19}$
$\sigma_{\text{ground-r}}$	$\mathcal{J}(0.1, 1000)$	$989.77^{+2.35}_{-0.83}$
$\sigma_{\text{GP,TESS-S9}}$	$\mathcal{J}(10^{-8}, 1000)$	$6.90e-4^{+14.51e-4}_{-3.19e-4}$
$\sigma_{\text{GP,TESS-S10}}$	$\mathcal{J}(10^{-8}, 1000)$	$9.10e-4^{+18.37e-4}_{-5.34e-4}$
$\sigma_{\text{GP,TESS-S63}}$	$\mathcal{J}(10^{-8}, 1000)$	$0.18e-4^{+2.74e-4}_{-0.17e-4}$
$\sigma_{\text{GP,TESS-S90}}$	$\mathcal{J}(10^{-8}, 1000)$	$9.33e-4^{+0.49e-4}_{-1.14e-4}$
$\rho_{\text{GP,TESS-S9}}$	$\mathcal{J}(0.001, 1000)$	$1.66^{+1.63}_{-0.85}$
$\rho_{\text{GP,TESS-S10}}$	$\mathcal{J}(0.001, 1000)$	$2.76^{+2.66}_{-1.33}$
$\rho_{\text{GP,TESS-S63}}$	$\mathcal{J}(0.001, 1000)$	$1.08^{+0.37}_{-0.94}$
$\rho_{\text{GP,TESS-S90}}$	$\mathcal{J}(0.001, 1000)$	$1.13^{+0.38}_{-0.35}$

eccentric orbit ($e = 0.43$) with an orbital period of 21.6 days. Having a mass of $0.51 M_J$ and a radius of $0.97 R_J$, its bulk density is therefore less than 800 kg/m^3 . The third detected planet, TIC 87422071b, has a mass of $1.29 M_J$ and orbits its parent star in 11.4 days. Due to a smaller distance from a star, its equilibrium temperature is slightly above 1100 K, which is still consistent with the population of warm Jupiter planets.

Figure 12 shows the population of warm giant exoplanets in a mass-radius diagram. All three planets presented in this study are uninflated and close to the bulk density level of 1 g/cm^3 . These new exoplanets lie in a sparsely populated region of the period-radius diagram (Fig. 13), corresponding to warm Jupiter planets with orbital periods greater than 10 days. Additionally, TIC 245076932b has a moderately eccentric orbit (see Fig. 14). The other two planets of this study have nearly circular orbits more frequent in the known sample of warm Jupiters.

The population of warm giant planets is also interesting for performing future atmospheric characterisation (e.g. Bello-Arufe et al. 2025), and linking atmospheric composition with possible formation channels. According to our interior structure modelling, the three planets presented in this study are significantly enriched in heavy elements, and these could translate into high abundances of C, N, and O dominated molecules. We fol-

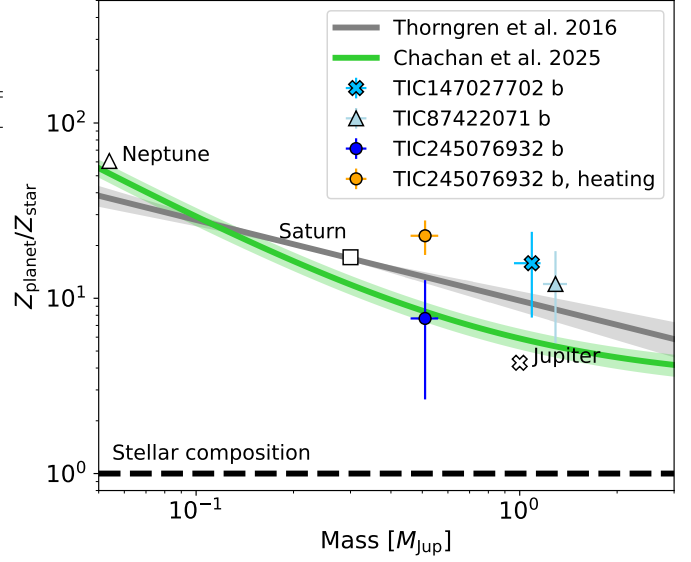


Fig. 11. Mass-bulk metal mass fraction diagram for the three exoplanets. We show Neptune, Saturn and Jupiter (Miguel & Vazan 2023, and references therein) as well as the exoplanet trends fitted by Thorngren et al. (2016) and Chachan et al. (2025).

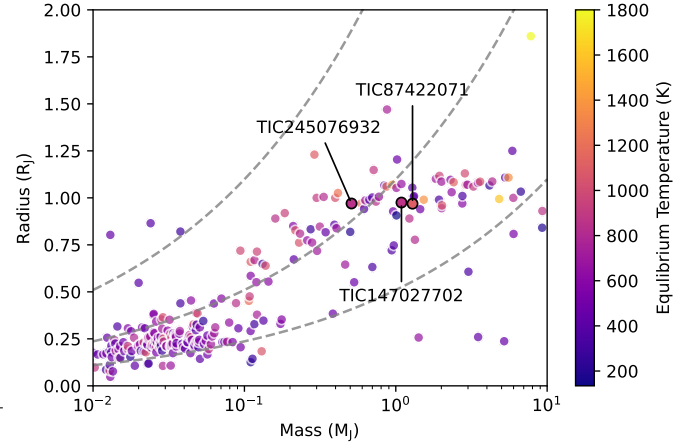


Fig. 12. Mass-radius diagram for the population of warm giant planets ($P > 10$ days). Dashed lines correspond to bulk densities of 0.1 g/cm^3 , 1 g/cm^3 , and 10 g/cm^3 (from top to bottom).

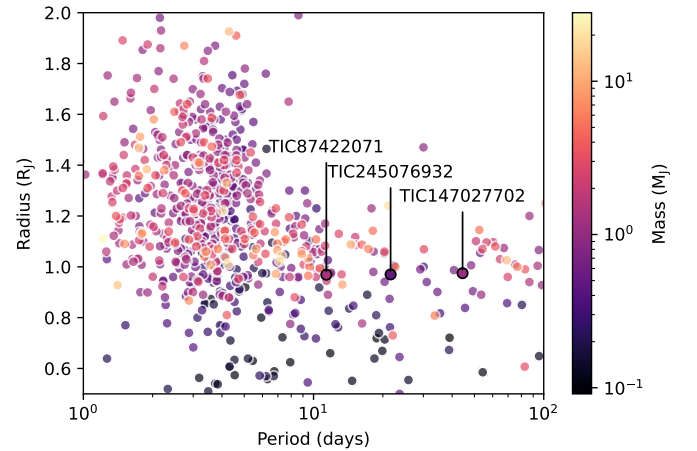


Fig. 13. Period-radius diagram for the population of giant planets ($M > 0.1 M_J$).

Table 3. Prior parameter distributions for TIC 245076932. For detail description see Tab. 2.

Parameter	Distribution	Value
P (days)	$\mathcal{N}(21.614, 0.2)$	$21.613890 \pm 1.7e-5$
$t_0 - 2457000$ (days)	$\mathcal{N}(2357.6, 0.2)$	$2357.66168^{+1.19e-3}_{-1.26e-3}$
$b \equiv a/R_\star \cos i$	$\mathcal{U}(0, 1)$	$0.106^{+0.106}_{-0.068}$
$p \equiv R_p/R_\star$	$\mathcal{U}(0.001, 0.1)$	0.0774 ± 0.0004
$e \sin \omega$	$\mathcal{U}(-0.8, 0.8)$	$-0.386^{+0.008}_{-0.016}$
$e \cos \omega$	$\mathcal{U}(-0.8, 0.8)$	$0.182^{+0.026}_{-0.030}$
ρ_\star (kg/m ³)	$\mathcal{N}(740, 60)$	$736.66^{+1.82}_{-1.32}$
K (m/s)	$\mathcal{U}(0, 100)$	$38.53^{+1.51}_{-1.93}$
$\mu_{\text{PlatoSpec}}$ (m/s)	$\mathcal{U}(-6000, -3000)$	$-4169.24^{+2.87}_{-2.17}$
$\sigma_{\text{PlatoSpec}}$ (m/s)	$\mathcal{J}(0, 1000)$	$20.57^{+1.13}_{-1.66}$
$q_{1,\text{TESS}}$	$\mathcal{U}(0, 1)$	$0.24^{+0.15}_{-0.10}$
$q_{2,\text{TESS}}$	$\mathcal{U}(0, 1)$	$0.23^{+0.28}_{-0.15}$
$q_{1,\text{ground-B}}$	$\mathcal{U}(0, 1)$	$0.20^{+0.04}_{-0.03}$
$q_{2,\text{ground-B}}$	$\mathcal{U}(0, 1)$	$0.87^{+0.09}_{-0.12}$
$q_{1,\text{ground-R}}$	$\mathcal{U}(0, 1)$	$0.008^{+0.012}_{-0.005}$
$q_{2,\text{ground-R}}$	$\mathcal{U}(0, 1)$	$0.61^{+0.30}_{-0.35}$
$\mu_{\text{TESS-S11}}$	$\mathcal{N}(0, 0.1)$	$-9.33e-4^{+14.9e-4}_{-5.96e-4}$
$\mu_{\text{TESS-S37}}$	$\mathcal{N}(0, 0.1)$	$0.182^{+0.066}_{-0.058}$
$\mu_{\text{TESS-S38}}$	$\mathcal{N}(0, 0.1)$	$-4.11e-4^{+9.19e-4}_{-6.75e-4}$
$\mu_{\text{TESS-S64}}$	$\mathcal{N}(0, 0.1)$	$0.149^{+0.057}_{-0.048}$
$\mu_{\text{ground-B}}$	$\mathcal{N}(0, 0.1)$	$-6.17e-4^{+0.35e-4}_{-0.32e-4}$
$\mu_{\text{ground-R}}$	$\mathcal{N}(0, 0.1)$	$-0.19e-4^{+0.63e-4}_{-0.61e-4}$
$\sigma_{\text{TESS-S11}}$	$\mathcal{J}(0.1, 1000)$	$5.18^{+2.88}_{-4.04}$
$\sigma_{\text{TESS-S37}}$	$\mathcal{J}(0.1, 1000)$	$4.28^{+2.82}_{-3.87}$
$\sigma_{\text{TESS-S38}}$	$\mathcal{J}(0.1, 1000)$	$4.86^{+3.84}_{-3.54}$
$\sigma_{\text{TESS-S64}}$	$\mathcal{J}(0.1, 1000)$	$5.10^{+4.45}_{-4.07}$
$\sigma_{\text{ground-B}}$	$\mathcal{J}(0.1, 1000)$	$15.18^{+2.03}_{-2.55}$
$\sigma_{\text{ground-R}}$	$\mathcal{J}(0.1, 1000)$	$14.93^{+2.13}_{-1.89}$
$\sigma_{\text{GP,TESS-S11}}$	$\mathcal{J}(10^{-8}, 1000)$	$9.78e-4^{+39.13e-4}_{-4.33e-4}$
$\sigma_{\text{GP,TESS-S37}}$	$\mathcal{J}(10^{-8}, 1000)$	$0.108^{+0.0987}_{-0.039}$
$\sigma_{\text{GP,TESS-S38}}$	$\mathcal{J}(10^{-8}, 1000)$	$16.25e-4^{+0.0134}_{-10.93e-4}$
$\sigma_{\text{GP,TESS-S64}}$	$\mathcal{J}(10^{-8}, 1000)$	$0.093^{+0.082}_{-0.035}$
$\rho_{\text{GP,TESS-S11}}$	$\mathcal{J}(0.001, 1000)$	$0.71^{+1.67}_{-0.46}$
$\rho_{\text{GP,TESS-S37}}$	$\mathcal{J}(0.001, 1000)$	$34.95^{+2.56}_{-2.97}$
$\rho_{\text{GP,TESS-S38}}$	$\mathcal{J}(0.001, 1000)$	$1.37^{+2.90}_{-1.03}$
$\rho_{\text{GP,TESS-S64}}$	$\mathcal{J}(0.001, 1000)$	$39.17^{+3.55}_{-2.79}$

Table 4. Prior parameter distributions for TIC 87422071. For detail description see Tab. 2.

Parameter	Distribution	Value
P (days)	$\mathcal{N}(11.365, 0.2)$	$11.364929^{+0.21e-4}_{-0.22e-4}$
$t_0 - 2457000$ (days)	$\mathcal{N}(1680.7, 0.2)$	$1680.65985^{+2.58e-3}_{-2.84e-3}$
$b \equiv a/R_\star \cos i$	$\mathcal{U}(0, 1)$	$0.718^{+0.073}_{-0.102}$
$p \equiv R_p/R_\star$	$\mathcal{U}(0.001, 0.1)$	$0.0669^{+0.0027}_{-0.0027}$
$e \sin \omega$	$\mathcal{U}(-0.8, 0.8)$	$0.056^{+0.116}_{-0.114}$
$e \cos \omega$	$\mathcal{U}(-0.8, 0.8)$	$0.046^{+0.067}_{-0.071}$
ρ_\star (kg/m ³)	$\mathcal{N}(530, 50)$	$530.57^{+2.11}_{-1.80}$
K (m/s)	$\mathcal{U}(0, 200)$	$101.63^{+3.13}_{-3.40}$
$\mu_{\text{PlatoSpec}}$ (m/s)	$\mathcal{U}(1000, 3000)$	$2759.65^{+2.14}_{-2.76}$
$\sigma_{\text{PlatoSpec}}$ (m/s)	$\mathcal{J}(0, 1000)$	$44.95^{+1.62}_{-1.95}$
μ_{FEROS} (m/s)	$\mathcal{U}(1000, 3000)$	$2735.61^{+3.28}_{-3.11}$
σ_{FEROS} (m/s)	$\mathcal{J}(0, 1000)$	$34.94^{+3.09}_{-2.50}$
$q_{1,\text{TESS}}$	$\mathcal{U}(0, 1)$	$0.22^{+0.27}_{-0.15}$
$q_{2,\text{TESS}}$	$\mathcal{U}(0, 1)$	$0.47^{+0.40}_{-0.33}$
$q_{1,\text{ground-g}}$	$\mathcal{U}(0, 1)$	$0.65^{+0.22}_{-0.30}$
$q_{2,\text{ground-g}}$	$\mathcal{U}(0, 1)$	$0.51^{+0.29}_{-0.35}$
$q_{1,\text{ground-r}}$	$\mathcal{U}(0, 1)$	$0.63^{+0.26}_{-0.33}$
$q_{2,\text{ground-r}}$	$\mathcal{U}(0, 1)$	$0.66^{+0.24}_{-0.39}$
$q_{1,\text{ground-i}}$	$\mathcal{U}(0, 1)$	$0.43^{+0.39}_{-0.29}$
$q_{2,\text{ground-i}}$	$\mathcal{U}(0, 1)$	$0.35^{+0.37}_{-0.26}$
$\mu_{\text{TESS-S13}}$	$\mathcal{N}(0, 0.1)$	$0.0015^{+0.0027}_{-0.0025}$
$\mu_{\text{TESS-S66}}$	$\mathcal{N}(0, 0.1)$	$0.3361^{+0.0846}_{-0.0865}$
$\mu_{\text{TESS-S93}}$	$\mathcal{N}(0, 0.1)$	$-0.64e-4^{+2.14e-4}_{-1.38e-4}$
$\mu_{\text{ground-g}}$	$\mathcal{N}(0, 0.1)$	$0.78e-4^{+1.82e-4}_{-1.80e-4}$
$\mu_{\text{ground-r}}$	$\mathcal{N}(0, 0.1)$	$5.64e-4^{+3.06e-4}_{-3.09e-4}$
$\mu_{\text{ground-i}}$	$\mathcal{N}(0, 0.1)$	$0.59e-4^{+1.92e-4}_{-2.01e-4}$
$\sigma_{\text{TESS-S13}}$	$\mathcal{J}(0.1, 1000)$	$9.52^{+2.13}_{-2.68}$
$\sigma_{\text{TESS-S66}}$	$\mathcal{J}(0.1, 1000)$	$997.07^{+1.89}_{-1.97}$
$\sigma_{\text{TESS-S93}}$	$\mathcal{J}(0.1, 1000)$	$4.21^{+1.92}_{-3.79}$
$\sigma_{\text{ground-g}}$	$\mathcal{J}(0.1, 1000)$	$40.57^{+1.95}_{-2.39}$
$\sigma_{\text{ground-r}}$	$\mathcal{J}(0.1, 1000)$	$40.65^{+3.03}_{-3.12}$
$\sigma_{\text{ground-i}}$	$\mathcal{J}(0.1, 1000)$	$40.73^{+2.42}_{-2.28}$
$\sigma_{\text{GP,TESS-S13}}$	$\mathcal{J}(10^{-8}, 1000)$	$0.0038^{+0.0034}_{-0.0012}$
$\sigma_{\text{GP,TESS-S66}}$	$\mathcal{J}(10^{-8}, 1000)$	$0.1749^{+0.1732}_{-0.0665}$
$\sigma_{\text{GP,TESS-S93}}$	$\mathcal{J}(10^{-8}, 1000)$	$1.07e-4^{+61.13e-4}_{-1.02e-4}$
$\rho_{\text{GP,TESS-S13}}$	$\mathcal{J}(0.001, 1000)$	$1.35^{+0.85}_{-0.43}$
$\rho_{\text{GP,TESS-S66}}$	$\mathcal{J}(0.001, 1000)$	$537.36^{+3.74}_{-3.38}$
$\rho_{\text{GP,TESS-S93}}$	$\mathcal{J}(0.001, 1000)$	$11.51^{+2.38}_{-1.79}$

lowed Kempton et al. (2018) to calculate the transmission spectroscopy metric (TSM) and the emission spectroscopy metric (ESM). The TSM values of TIC 147027702b, TIC 245076932b, and TIC 87422071b are 7.3 ± 3.3 , 35.6 ± 13.7 and 12.8 ± 6.5 , respectively. TIC 245076932b appears to be the best candidate for transmission spectroscopy, but is still hardly reachable using JWST/NIRISS (Doyon et al. 2023). However, this planet seems to be a suitable target for future instruments such as ARIEL (Edwards & Tinetti 2022) or ELT/ANDES (Palle et al. 2025). The ESM values are 5.3 ± 0.9 (TIC 147027702b), 13.2 ± 1.6 (TIC 245076932b), and 16.6 ± 3.0 (TIC 87422071b).

A crucial observable for constraining the origin and orbital evolution of warm Jupiters is the inclination of the orbit with respect to the rotation axis of the parent star (stellar obliquity). The projected stellar obliquity can be measured by observing the Rossiter-McLaughlin (RM) effect during transit (e.g. Zak et al. 2025b). All three stars in the present study are slow rotators. Therefore, the predicted maximal amplitude of the RM effect (i.e. for aligned orbits) is in the range of 18–25 m/s, which would

be suitable for instruments like HARPS and ESPRESSO. The significant eccentricity of TIC 245076932b, makes it an interesting object to measure its stellar obliquity, given that some high-eccentricity migration mechanisms predict significant misalignments (Petrovich & Tremaine 2016). Recent studies targeting moderately eccentric ($\sim 0.3 - 0.6$) warm Jupiters (e.g. Espinoza-Retamal et al. 2025; Zak et al. 2025a), are showing a tentative trend in the opposite direction, where several mechanisms were proposed to explain the origin of this sub-population of warm Jupiters.

Expanding the sample of well-characterised warm Jupiters, including the three systems presented here, will be essential to disentangle the possible theories of warm- and hot Jupiter planet formation and to place robust constraints on the dominant evolutionary mechanisms at intermediate orbital periods.

Acknowledgements. We would like to thank L. Řezba, M. Skarka, and J. Šubjak for performing observations of these targets. This work makes use of observa-

Table 5. Fitted and derived planetary parameters of all systems.

	TIC 147027702	TIC 245076932	TIC 87422071
P (days)	44.40523 ± 0.00013	21.613890 ± 0.000017	$11.364929^{+0.000021}_{-0.000022}$
t_0 (days)	$2458550.7314^{+0.0035}_{-0.0038}$	$2459357.6617^{+0.0012}_{-0.0013}$	$2458680.6599^{+0.0026}_{-0.0028}$
$b \equiv a/R_\star \cos i$	$0.230^{+0.145}_{-0.155}$	$0.106^{+0.106}_{-0.068}$	$0.718^{+0.073}_{-0.102}$
$p \equiv R_p/R_\star$	$0.0469^{+0.0009}_{-0.0010}$	0.0774 ± 0.0004	$0.0669^{+0.0027}_{-0.0027}$
e	$0.127^{+0.055}_{-0.048}$	$0.428^{+0.022}_{-0.019}$	$0.124^{+0.073}_{-0.060}$
ω (deg)	$223.7^{+22.5}_{-17.4}$	$295.0^{+2.6}_{-3.3}$	$46.4^{+51.9}_{-93.6}$
ρ_\star (kg/m ³)	$201.55^{+3.67}_{-2.17}$	$736.66^{+1.82}_{-1.32}$	$530.57^{+2.11}_{-1.80}$
K (m/s)	$50.43^{+1.36}_{-3.61}$	$38.53^{+1.51}_{-1.93}$	$101.63^{+3.13}_{-3.40}$
i (deg)	$89.52^{+0.32}_{-0.30}$	$89.77^{+0.15}_{-0.23}$	$87.32^{+0.38}_{-0.27}$
M_p (M _J)	$1.09^{+0.07}_{-0.13}$	$0.51^{+0.04}_{-0.05}$	$1.29^{+0.10}_{-0.11}$
a (au)	$0.274^{+0.014}_{-0.013}$	0.157 ± 0.007	0.106 ± 0.005
R_p (R _J)	$0.975^{+0.065}_{-0.064}$	0.970 ± 0.048	$0.969^{+0.087}_{-0.084}$
ρ_p (kg/m ³)	$1566.6^{+488.2}_{-426.5}$	$746.6^{+48.7}_{-55.9}$	$1878.5^{+330.2}_{-284.21}$
g_p (m/s ²)	29.9 ± 6.7	$14.2^{+2.9}_{-2.6}$	$35.6^{+10.4}_{-8.3}$
T_{eq} (K)	863^{+26}_{-27}	845 ± 25	1110 ± 33
$\delta \equiv p^2$ (%)	0.220 ± 0.009	0.599 ± 0.006	$0.447^{+0.036}_{-0.037}$
T_{14} (hours)	$15.9^{+0.9}_{-1.8}$	9.2 ± 0.5	$3.6^{+1.7}_{-0.8}$
T_{23} (hours)	$14.4^{+0.9}_{-1.8}$	7.9 ± 0.4	$2.8^{+1.4}_{-0.9}$

Table 6. Interior composition parameters retrieved by our interior structure retrievals.

	TIC 147027702 b	TIC 245076932 b	TIC 245076932 b, heating	TIC 87422071
Core Mass Fraction, CMF	$0.16^{+0.11}_{-0.16}$	$0.09^{+0.09}_{-0.06}$	$0.33^{+0.08}_{-0.10}$	$0.21^{+0.16}_{-0.12}$
Core Mass, M_{core} [M _⊕]	55.9 ± 34.0	16.4 ± 12.4	50.1 ± 16.3	92.0 ± 58.5
Envelope metal mass fraction, Z_{env}	$0.01^{+0.07}_{-0.01}$	$0.01^{+0.04}_{-0.01}$	$0.01^{+0.10}_{-0.01}$	$0.01^{+0.08}_{-0.01}$
Internal temperature, T_{int} [K]	141^{+25}_{-26}	86^{+11}_{-10}	350 (constant)	148 ± 31
Bulk metal mass fraction, Z_{planet}	$0.19^{+0.11}_{-0.09}$	$0.11^{+0.09}_{-0.07}$	0.36 ± 0.07	$0.25^{+0.16}_{-0.12}$
Planet-to-star bulk metal mass fraction ratio, $Z_{\text{planet}}/Z_{\text{star}}$	15.85 ± 8.09	7.67 ± 5.02	22.73 ± 5.06	12.06 ± 6.51

Table 7. Interior composition parameters from MESA.

	TIC 147027702 b	TIC 87422071
Core Mass Fraction, CMF	$0.16^{+0.07}_{-0.09}$	$0.13^{+0.13}_{-0.13}$
Core Mass, M_{core} [M _⊕]	$56.0^{+24.0}_{-32.0}$	$55.0^{+55.0}_{-55.0}$
Envelope metal mass fraction, Z_{env}	0.013	0.038
Core density [g/cm ³]	9.5	11.0
Bulk metal mass fraction, Z_{planet}	$0.17^{+0.07}_{-0.09}$	$0.17^{+0.13}_{-0.13}$
Planet-to-star bulk metal mass fraction ratio, $Z_{\text{planet}}/Z_{\text{star}}$	$13.4^{+5.5}_{-7.1}$	$7.6^{+5.9}_{-5.9}$

tions from the LCOGT network. Part of the LCOGT telescope time was granted by NOIRLab through the Mid-Scale Innovations Program (MSIP). The MSIP is funded by NSF. This research has used the website of the Exoplanet Follow-up Observation Programme (ExoFOP; DOI: 10.26134/ExoFOP5), which is operated by the California Institute of Technology, under contract with the National Aeronautics and Space Administration under the Exoplanet Exploration Programme. Funding for the TESS mission is provided by NASA's Science Mission Directorate. KAC acknowledges support from the TESS mission via sub-award s3449 from MIT. We would like to acknowledge the dedicated staff of the French and Italian polar agencies (IPEV and PNRA) for their dedication and for their work, particularly those who winter-over, which is essential in maintaining the Concordia Station operational throughout the Austral winter, and thanks to whom the ASTEP+ telescope could collect data for this publication. ASTEP+ benefited from the support of the French and Italian polar agencies IPEV and PNRA in the framework of the Concordia station programme, from OCA, INSU, Idex UCAJEDI (ANR-15-IDEX-01) and ESA through the Science Faculty of the European Space Research and Technology Centre (ESTEC). ASTEP+ also received funding through the Science and Technology Facilities Council (STFC; grants n° ST/S00193X/1, ST/W002582/1 and ST/Y001710/1) as well as the European Research Council (ERC) under the Horizon 2020 research and innovation programme of the European Union (grant agreement n° 803193/BEBOP). This work was supported by the Slovak Research and Development Agency un-

der contract No. APVV-24-0160, and by the Ministry of Education, Youth and Sports of the Czech Republic by grant LTT-20015. The research of P.G. was supported by the internal grant No. VVGS-2023-2784 of the P. J. Šafárik University in Košice and funded by the EU NextGenerationEU through the Recovery and Resilience Plan for Slovakia under project No. 09I03-03-V05-00008. Funding for KB was provided by the European Union (ERC AdG SUBSTELLAR, GA 101054354). JJ is grateful that publication could be produced within the institutional support framework for the development of the research organisation of Masaryk University.

References

- Acuña, L., Deleuil, M., Mousis, O., et al. 2021, *A&A*, 647, A53
Acuña, L., Kreidberg, L., Zhai, M., & Mollière, P. 2024, *A&A*, 688, A60
Acuña, L., Kreidberg, L., Zhai, M., Mollière, P., & Fouesneau, M. 2025, *The Journal of Open Source Software*, 10, 7288
Aller, A., Lillo-Box, J., Jones, D., Miranda, L. F., & Barceló Forteza, S. 2020, *A&A*, 635, A128
Ambikasaran, S., Foreman-Mackey, D., Greengard, L., Hogg, D. W., & O'Neil, M. 2015, *IEEE Transactions on Pattern Analysis and Machine Intelligence*, 38, 252

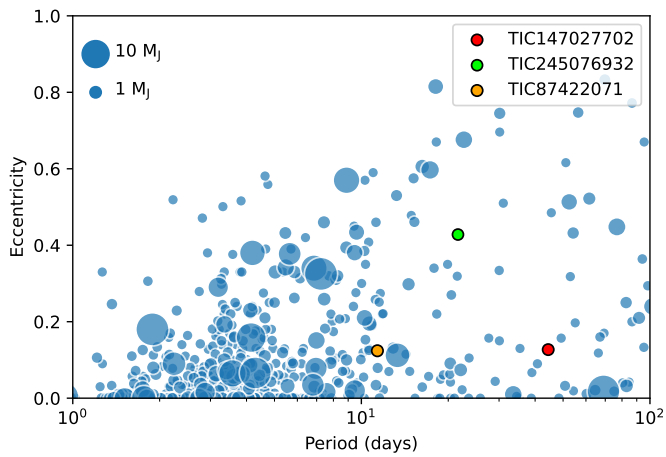


Fig. 14. Period-eccentricity diagram for the population of transiting giant planets ($M > 0.1 M_J$).

Barat, S., Désert, J.-M., Mukherjee, S., et al. 2025, *AJ*, 170, 165
 Batygin, K. 2025, *ApJ*, 985, 87
 Bello-Arufe, A., Hu, R., Zilinskas, M., et al. 2025, arXiv e-prints, arXiv:2511.15835
 Brahm, R., Espinoza, N., Jordán, A., et al. 2019, *AJ*, 158, 45
 Brahm, R., Jordán, A., & Espinoza, N. 2017a, *PASP*, 129, 034002
 Brahm, R., Jordán, A., Hartman, J., & Bakos, G. 2017b, *MNRAS*, 467, 971
 Brahm, R., Ulmer-Moll, S., Hobson, M. J., et al. 2023, *AJ*, 165, 227
 Bressan, A., Marigo, P., Girardi, L., et al. 2012, *MNRAS*, 427, 127
 Brown, T. M., Baliber, N., Bianco, F. B., et al. 2013, *PASP*, 125, 1031
 Chachan, Y., Fortney, J. J., Ohno, K., Thorngren, D., & Murray-Clay, R. 2025, *ApJ*, 994, 43
 Collins, K. A., Kielkopf, J. F., Stassun, K. G., & Hessman, F. V. 2017, *AJ*, 153, 77
 Danti, C., Bitsch, B., & Mah, J. 2023, *A&A*, 679, L7
 Dong, J., Huang, C. X., Dawson, R. I., et al. 2021, *ApJS*, 255, 6
 Dorn, C., Khan, A., Heng, K., et al. 2015, *A&A*, 577, A83
 Doyon, R., Willott, C. J., Hutchings, J. B., et al. 2023, *PASP*, 135, 098001
 Dransfield, G., Mékarnia, D., Triaud, A. H. M. J., et al. 2022, in Society of Photo-Optical Instrumentation Engineers (SPIE) Conference Series, Vol. 12186, *Observatory Operations: Strategies, Processes, and Systems IX*, ed. D. S. Adler, R. L. Seaman, & C. R. Benn, 121861F
 Eberhardt, J., Hobson, M. J., Henning, T., et al. 2023, *AJ*, 166, 271
 Edwards, B. & Tinetti, G. 2022, *AJ*, 164, 15
 Espinoza, N., Kossakowski, D., & Brahm, R. 2019, *MNRAS*, 490, 2262
 Espinoza-Retamal, J. I., Jordán, A., Brahm, R., et al. 2025, *AJ*, 170, 70
 Feinstein, A. D., Booth, R. A., Bergner, J. B., et al. 2025, arXiv e-prints, arXiv:2506.00669
 Foreman-Mackey, D., Agol, E., Ambikasaran, S., & Angus, R. 2017, *AJ*, 154, 220
 Foreman-Mackey, D., Hogg, D. W., Lang, D., & Goodman, J. 2013, *PASP*, 125, 306
 Fulton, B. J., Petigura, E. A., Blunt, S., & Sinukoff, E. 2018, *PASP*, 130, 044504
 Gaia Collaboration. 2023, *A&A*, 674, A1
 Hobson, M. J., Trifonov, T., Henning, T., et al. 2023, *AJ*, 166, 201
 Huang, C. X., Vanderburg, A., Pál, A., et al. 2020, *Research Notes of the American Astronomical Society*, 4, 204
 Hubbard, W. B. & Marley, M. S. 1989, *Icarus*, 78, 102
 Jones, M. I., Reinartz, Y., Brahm, R., et al. 2024, *A&A*, 683, A192
 Jordán, A., Brahm, R., Espinoza, N., et al. 2020, *AJ*, 159, 145
 Kabáth, P., Skarka, M., Hatzes, A., et al. 2026, *MNRAS*, 545, staf1972
 Kaufer, A., Stahl, O., Tubbesing, S., et al. 1999, *The Messenger*, 95, 8
 Kempton, E. M.-R., Bean, J. L., Louie, D. R., et al. 2018, *PASP*, 130, 114401
 Kley, W. & Nelson, R. P. 2012, *ARA&A*, 50, 211
 Kreidberg, L. 2015, *PASP*, 127, 1161
 Leconte, J., Chabrier, G., Baraffe, I., & Levrard, B. 2010, *A&A*, 516, A64
 McCully, C., Volgenau, N. H., Harbeck, D.-R., et al. 2018, in Society of Photo-Optical Instrumentation Engineers (SPIE) Conference Series, Vol. 10707, *Proc. SPIE*, 107070K
 Mékarnia, D., Guillot, T., Rivet, J. P., et al. 2016, *MNRAS*, 463, 45
 Miguel, Y. & Vazan, A. 2023, *Remote Sensing*, 15, 681
 Millholland, S., Petigura, E., & Batygin, K. 2020, *ApJ*, 897, 7
 Mollière, P., van Boekel, R., Bouwman, J., et al. 2017, *A&A*, 600, A10
 Mollière, P., van Boekel, R., Dullemond, C., Henning, T., & Mordasini, C. 2015, *ApJ*, 813, 47

Paegert, M., Stassun, K. G., Collins, K. A., et al. 2021, arXiv e-prints, arXiv:2108.04778
 Palle, E., Biazzo, K., Bolmont, E., et al. 2025, *Experimental Astronomy*, 59, 29
 Paxton, B., Bildsten, L., Dotter, A., et al. 2011, *ApJS*, 192, 3
 Paxton, B., Cantiello, M., Arras, P., et al. 2013, *ApJS*, 208, 4
 Petrovich, C. & Tremaine, S. 2016, *ApJ*, 829, 132
 Pollack, J. B., Hubickyj, O., Bodenheimer, P., et al. 1996, *Icarus*, 124, 62
 Rafikov, R. R. 2005, *ApJ*, 621, L69
 Ricker, G. R., Winn, J. N., Vanderspek, R., et al. 2015, *Journal of Astronomical Telescopes, Instruments, and Systems*, 1, 014003
 Rodríguez Martínez, R., Eastman, J. D., Collins, K. A., et al. 2025, *AJ*, 169, 72
 Salinas, H., Brahm, R., Olmschenk, G., et al. 2025, *MNRAS*, 538, 2031
 Santerne, A., Moutou, C., Tsantaki, M., et al. 2016, *A&A*, 587, A64
 Schlecker, M., Kossakowski, D., Brahm, R., et al. 2020, *AJ*, 160, 275
 Schlichting, H. E. 2014, *ApJ*, 795, L15
 Schmider, F.-X., Abe, L., Agabi, A., et al. 2022, in Society of Photo-Optical Instrumentation Engineers (SPIE) Conference Series, Vol. 12182, *Ground-based and Airborne Telescopes IX*, ed. H. K. Marshall, J. Spyromilio, & T. Usuda, 1218220
 Sing, D. K., Rustamkulov, Z., Thorngren, D. P., et al. 2024, *Nature*, 630, 831
 Tala Pinto, M., Jordán, A., Acuña, L., et al. 2025, *A&A*, 694, A268
 Tayar, J., Clayton, Z. R., Huber, D., & van Saders, J. 2022, *ApJ*, 927, 31
 Thorngren, D. P., Fortney, J. J., Murray-Clay, R. A., & Lopez, E. D. 2016, *ApJ*, 831, 64
 Trifonov, T., Brahm, R., Espinoza, N., et al. 2021, *AJ*, 162, 283
 Walsh, K. J., Morbidelli, A., Raymond, S. N., O'Brien, D. P., & Mandell, A. M. 2011, *Nature*, 475, 206
 Welbanks, L., Bell, T. J., Beatty, T. G., et al. 2024, *Nature*, 630, 836
 Wenger, M., Ochsenbein, F., Egret, D., et al. 2000, *A&AS*, 143, 9
 Zak, J., Boffin, H. M. J., Bocchieri, A., et al. 2025a, *AJ*, 170, 274
 Zak, J., Kabath, P., Boffin, H. M. J., et al. 2025b, *A&A*, 702, A266

Appendix A: Radial velocity observations

Table A.1. Radial-velocity data of TIC 147027702.

Time (BJD)	RV (m/s)	RV error (m/s)	SNR
2460686.7921940	22707.0	36.6	28
2460695.8248905	22678.4	24.0	45
2460695.8400650	22724.9	21.1	52
2460701.8156190	22764.0	22.1	49
2460702.8331103	22740.6	27.5	39
2460704.8489000	22816.8	27.4	39
2460710.8349756	22866.1	31.7	34
2460717.8033857	22724.9	38.7	27
2460721.8378543	22765.9	31.0	34
2460724.8093707	22757.4	20.3	54
2460731.7910830	22726.8	35.7	29
2460736.8218505	22680.3	21.9	50
2460738.8154537	22711.0	20.2	55
2460742.8102396	22751.7	30.0	35
2460743.7871938	22674.6	21.2	52
2460744.7619825	22753.9	22.0	50
2460745.7432980	22726.1	19.7	56
2460749.7804488	22785.0	25.8	43
2460751.8135311	22816.5	23.9	46
2460753.7393160	22780.7	21.2	52
2460757.7221696	22791.0	20.9	52
2460758.6920467	22773.2	41.7	25
2460760.6354317	22755.8	32.3	33
2460766.7161256	22826.8	18.8	59
2460768.7003831	22748.1	20.5	54
2460774.6598235	22682.9	30.2	36
2460778.7205240	22662.2	26.0	42
2460781.7031698	22708.6	19.3	58
2460783.6313187	22690.0	22.6	47
2460786.6357072	22674.1	35.3	30
2460786.6612736	22715.9	29.5	37
2460788.6784084	22748.2	19.3	58
2460790.6384807	22722.5	20.1	55
2460791.6160357	22786.9	21.1	51
2460792.6242137	22783.7	32.9	32
2460794.6346524	22688.5	23.1	47
2460797.6539720	22752.6	25.9	42
2460799.6221343	22780.0	27.2	34
2460798.6870562	22820.1	31.6	39
2460800.5909948	22732.4	25.7	41
2460805.6333315	22870.6	33.3	32
2460806.6896655	22744.1	27.6	40
2460807.5668869	22817.9	25.1	43
2460808.6134686	22774.7	23.4	47
2460809.5378564	22819.7	16.4	70
2460810.6896164	22697.5	31.7	35
2460815.6550418	22706.6	26.3	41
2460819.5596421	22741.3	27.8	38
2460823.5642501	22793.4	35.6	30
2460824.5241531	22704.4	19.5	57
2460825.6729563	22770.9	27.8	42
2460837.5533146	22785.3	25.6	43
2460848.5297432	22770.6	30.6	35
2460858.5583752	22669.7	30.8	36
2460865.5212450	22705.0	33.8	32

Appendix B: Activity indices

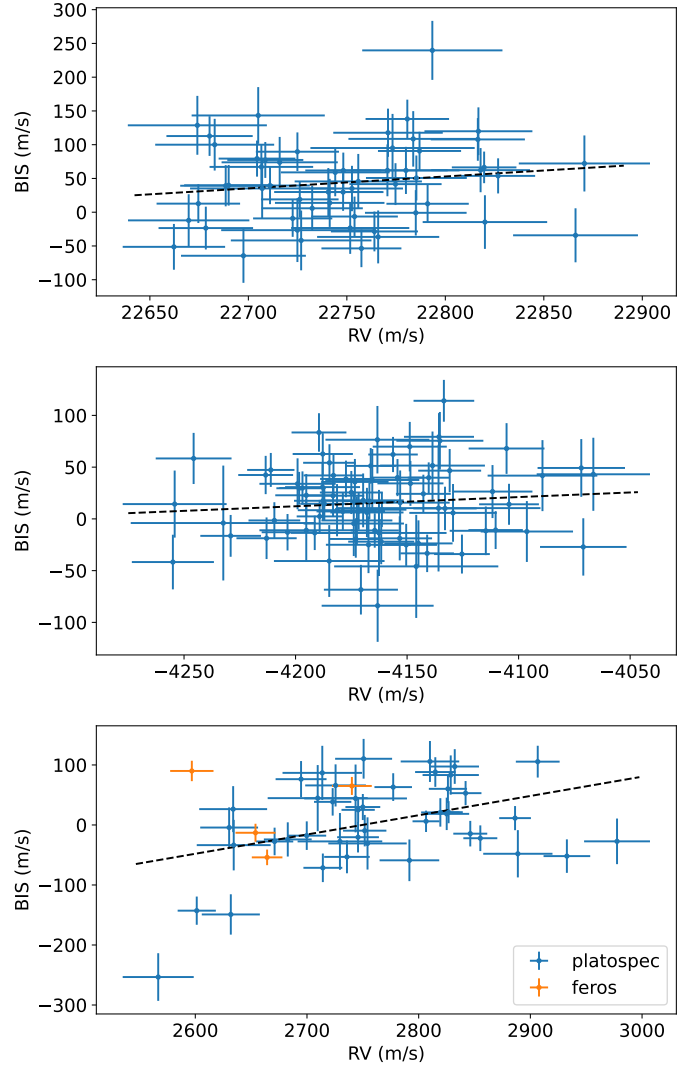


Fig. B.1. Bisector span (BIS) as a function of RV of TIC 147027702 (*top*), TIC 245076932 (*middle*) and TIC 87422071 (*bottom*). The dashed line shows the best linear fit to the data.

Appendix C: Corner plots

Table A.2. Radial-velocity data of TIC 245076932.

Time (BJD)	RV (m/s)	RV error (m/s)	SNR	Time (BJD)	RV (m/s)	RV error (m/s)	SNR
2460711.8505993	-4114.7	16.2	31	2460794.7420006	-4213.4	12.3	40
2460721.8684073	-4173.0	11.9	42	2460797.7424400	-4189.2	10.3	50
2460724.8308937	-4166.9	11.5	43	2460798.7707242	-4135.7	15.7	33
2460733.7977187	-4071.0	19.4	25	2460799.7252226	-4140.3	09.4	55
2460737.8368879	-4141.0	12.0	41	2460800.6578914	-4110.3	12.2	41
2460739.8316922	-4154.3	11.8	42	2460802.7360130	-4161.6	14.8	34
2460740.8550901	-4173.4	15.1	33	2460805.7193731	-4125.4	12.5	40
2460742.8645549	-4195.2	13.9	36	2460806.7745561	-4181.4	17.6	30
2460743.8506680	-4183.0	13.4	37	2460807.6433633	-4177.4	11.6	43
2460744.8476837	-4172.5	15.9	31	2460808.6857083	-4198.4	10.2	51
2460745.8530324	-4156.3	11.1	45	2460814.7840132	-4245.7	17.0	31
2460746.8913739	-4184.8	11.8	42	2460815.7354949	-4211.1	10.6	49
2460747.8593865	-4196.9	10.4	49	2460816.7158521	-4191.4	10.8	47
2460749.8505336	-4187.7	13.0	38	2460819.6696939	-4169.7	18.2	28
2460750.8608490	-4229.1	13.6	37	2460820.4827714	-4148.5	14.8	34
2460751.9015180	-4187.9	16.8	30	2460821.6545058	-4144.9	15.3	33
2460753.8357969	-4178.8	11.8	42	2460821.6828498	-4104.3	13.4	38
2460754.8381103	-4133.5	13.6	36	2460823.6058421	-4170.7	16.6	30
2460756.7853991	-4142.7	12.3	40	2460823.6349615	-4111.7	17.9	28
2460757.7892431	-4150.4	13.8	35	2460824.6128327	-4203.6	11.6	44
2460758.7420421	-4163.3	23.3	21	2460825.7411024	-4171.7	11.8	44
2460761.7903716	-4184.9	24.8	21	2460828.5918274	-4161.3	11.0	46
2460761.8182084	-4162.6	30.3	17	2460829.6110110	-4138.6	23.5	21
2460766.8173540	-4168.0	16.4	30	2460835.5910153	-4164.5	10.8	48
2460767.7971582	-4165.6	21.1	24	2460836.6383962	-4187.1	10.8	48
2460774.7592066	-4199.1	17.1	28	2460837.6614717	-4209.5	11.6	45
2460777.7719106	-4066.5	25.4	21	2460847.6477437	-4153.3	14.5	35
2460777.7938556	-4089.3	24.6	21	2460854.6321937	-4135.9	45.7	12
2460778.8181846	-4129.4	19.6	27	2460863.5972044	-4130.9	14.1	36
2460778.8469700	-4096.3	20.7	26	2460868.5748781	-4173.9	22.5	23
2460779.8045949	-4105.4	17.0	31	2460869.6238660	-4145.9	36.8	16
2460779.8324427	-4071.9	19.6	27	2460872.5404851	-4254.2	23.3	21
2460781.7800507	-4166.3	11.3	45	2460874.5620393	-4183.2	14.0	36
2460783.7382212	-4148.8	16.6	30	2460876.6452774	-4255.0	18.4	30
2460786.7501504	-4175.0	14.1	36	2460878.6032402	-4163.2	25.1	21
2460788.8115154	-4133.0	14.2	35	2460880.5676253	-4167.3	19.1	26
2460790.7512885	-4187.8	13.5	37	2460885.5648661	-4135.3	19.5	27
2460791.7542462	-4213.0	13.5	37	2460895.5209800	-4232.4	41.5	13
2460792.7106400	-4153.1	22.2	23	2460901.5866744	-4195.2	21.0	27
2460793.8391743	-4189.5	12.3	42				

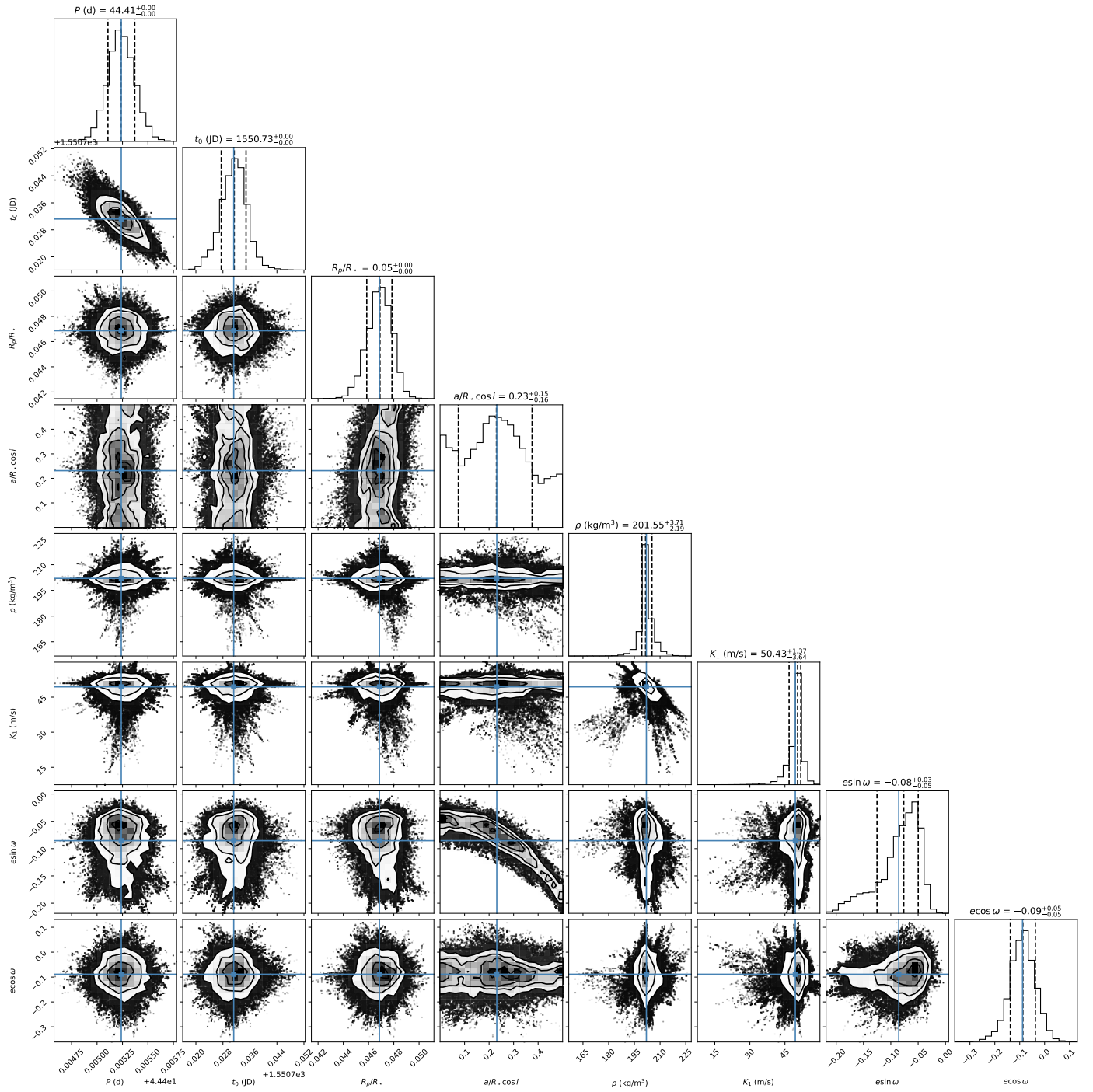


Fig. C.1. Corner plot showing posterior distributions and covariances for some fitted parameters in our analysis of TIC 147027702.

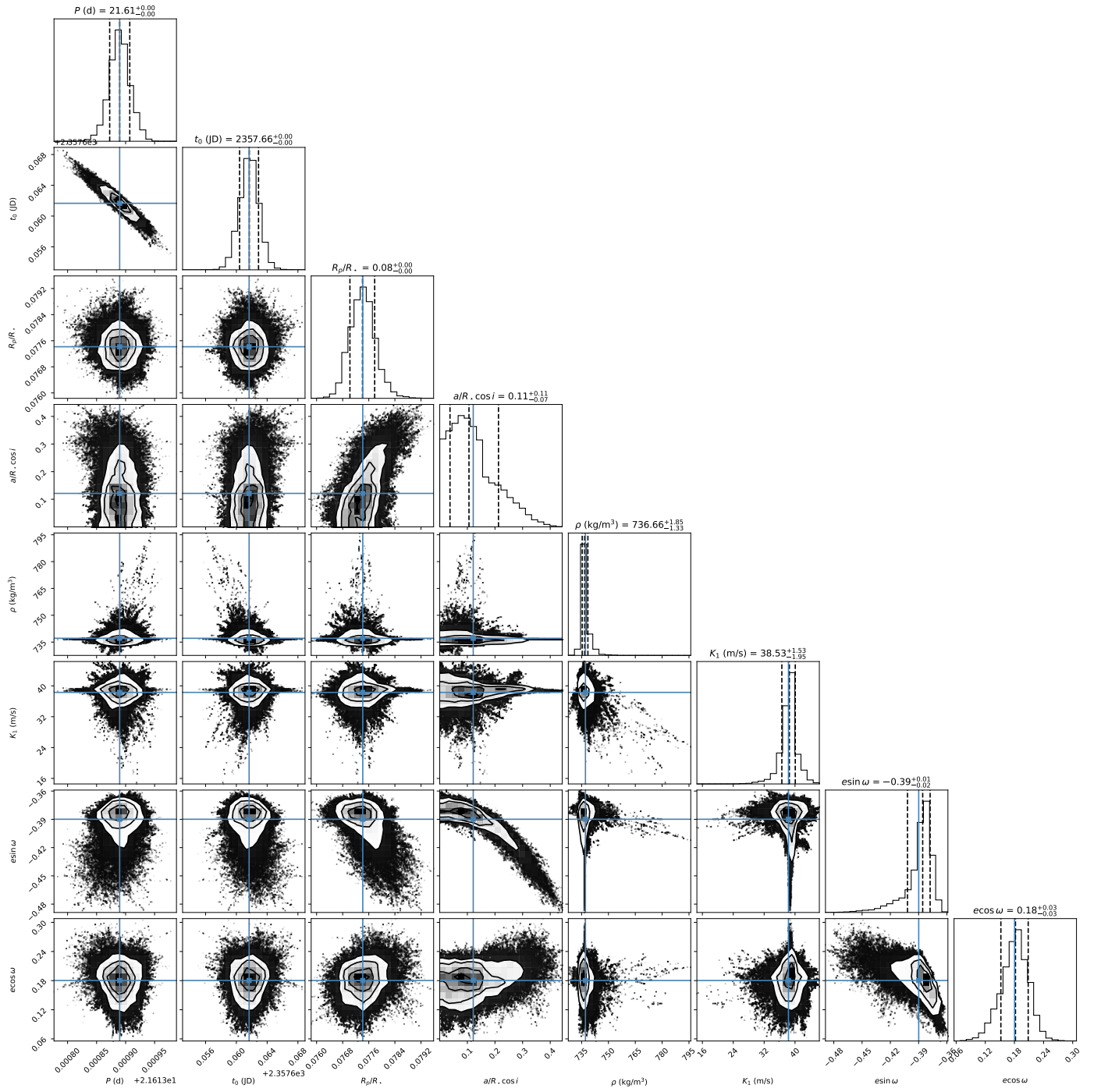


Fig. C.2. Corner plot showing posterior distributions and covariances for some fitted parameters in our analysis of TIC 245076932.

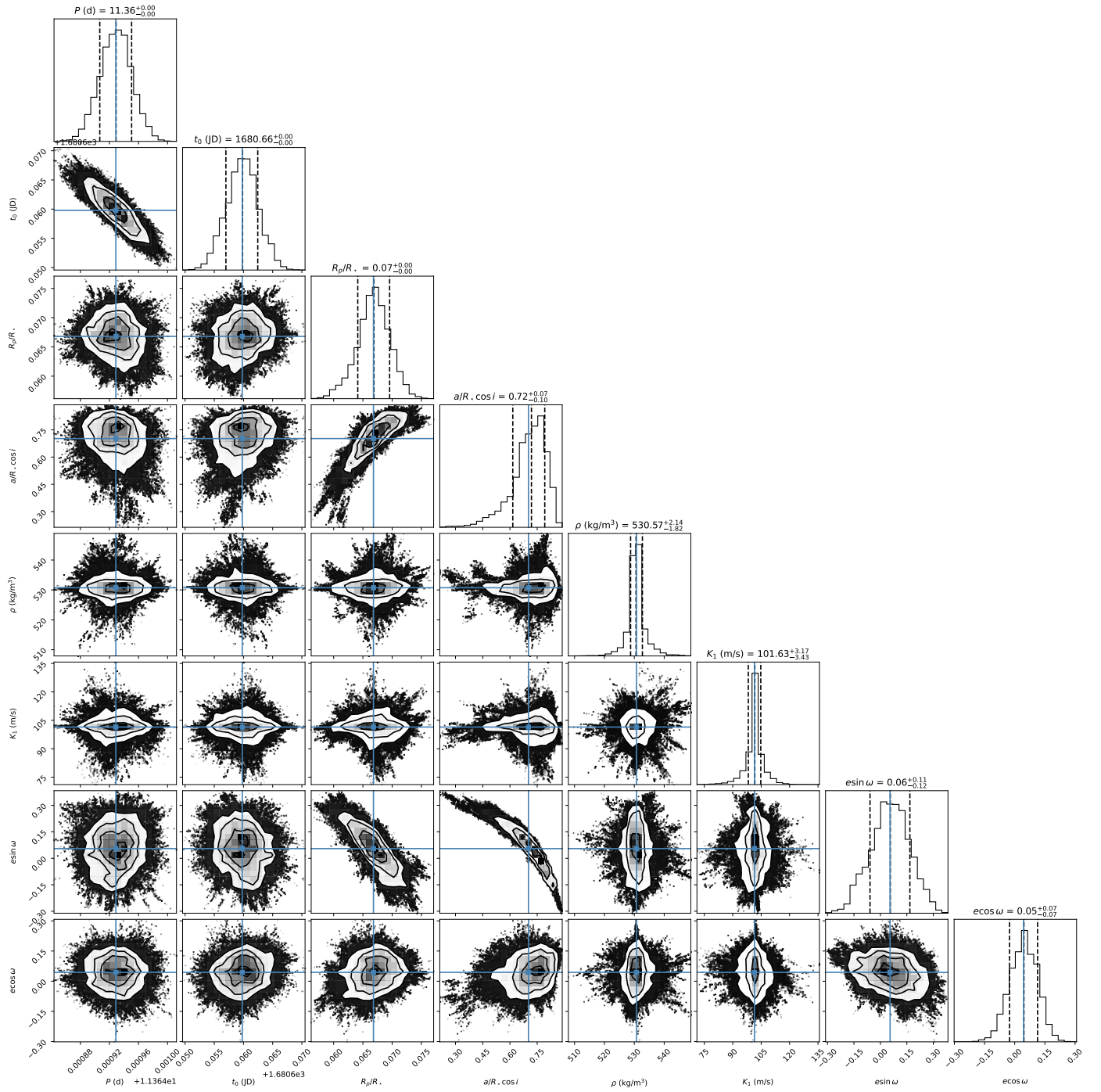


Fig. C.3. Corner plot showing posterior distributions and covariances for some fitted parameters in our analysis of TIC 87422071.

Table A.3. Radial-velocity data of TIC 87422071 obtained by PLATOSpec.

Time (BJD)	RV (m/s)	RV error (m/s)	SNR
2460805.8834210	2745.7	18.7	35
2460807.9155147	2694.7	22.8	29
2460808.8980161	2745.8	14.9	47
2460814.8751567	2906.6	19.6	34
2460815.8557630	2806.6	12.1	58
2460821.8501538	2810.1	26.2	26
2460823.7741806	2791.7	26.7	25
2460825.8367722	2855.2	15.2	44
2460826.8410798	2832.3	21.7	31
2460827.8000835	2826.8	12.7	54
2460828.7406824	2751.7	19.4	35
2460829.7904270	2743.5	46.0	16
2460831.8612531	2634.4	33.1	20
2460832.7799130	2713.7	35.6	19
2460835.7637607	2842.0	14.2	48
2460836.7780307	2932.7	20.9	32
2460837.7644513	2886.3	14.2	47
2460837.8028896	2977.6	29.5	23
2460847.6944565	2814.9	18.1	37
2460849.7573677	2729.5	37.9	18
2460854.7100868	2709.6	44.8	16
2460855.7134477	2725.6	27.2	25
2460857.7724212	2819.4	17.2	39
2460858.7063917	2888.8	31.0	22
2460858.7736015	2825.1	20.1	34
2460859.7045034	2846.2	15.2	45
2460861.7244720	2826.2	17.1	39
2460863.7033588	2682.8	21.4	32
2460864.6837203	2633.9	30.4	24
2460865.7026675	2601.3	17.1	40
2460867.6868202	2566.8	31.8	24
2460867.7146551	2631.8	26.0	27
2460868.6095502	2735.8	20.4	34
2460869.8269116	2754.2	35.1	22
2460872.6654226	2828.7	25.2	27
2460873.7521680	2777.2	16.8	40
2460876.7511659	2671.0	16.7	41
2460877.6283765	2630.3	25.9	26
2460878.6568412	2750.0	15.6	44
2460880.6843347	2750.7	25.5	26
2460885.7461869	2714.2	17.4	39
2460899.6580413	2699.8	17.4	38
2460913.5513713	2723.0	16.7	41

Table A.4. Radial-velocity data of TIC 87422071 obtained by FEROS.

Time (BJD)	RV (m/s)	RV error (m/s)	SNR
2460492.7845381	2740.2	17.8	45
2460501.7300205	2596.9	19.4	41
2460503.7693251	2653.9	17.9	45
2460831.8640888	2664.3	13.7	61